Development of a high-throughput 3D culture microfluidic platform for multi-parameter phenotypic and omics profiling of patient-derived organoids.

Oronza A. Botrugno[1,2]*^, Elena Bianchi[3]*^, Jolanda M. Bruno[2]#, Claudia Felici[2]#, Giovanni F.M. Gallo[2]#, Eduardo Sommella[4]#, Paola De Stefano[3], Valentina Giansanti[5], Valeria Rossella[5], Dejan Lazarevic[5], Fabrizio Merciai[4], Vicky Caponigro[4], Valentina Golino[4], Danila La Gioia[4], Antonio Malinconico[4], Emanuele Colombo[6], Giulio Giovannoni[2], Guido Gatti[2], Francesca Ratti[9], Silvia Buonanno[9], Federica Pedica[10], Carlo Tacchetti[1,7], Paola Falletta[1,7], Samuel Zambrano[1,8], Davide Mazza[1,7], Davide Cittaro[5], Pietro Campiglia[4], Luca Aldrighetti[9], Giovanni Tonon[1,2, 5]^ and Gabriele Dubini[3]^

1 Università Vita-Salute San Raffaele, Milano, Italy
2 Functional Genomics of Cancer Unit, Division of Experimental Oncology, IRCCS San Raffaele Scientific Institute, Milano, Italy.
3 Laboratory of Biological Structure Mechanics (LaBS), Department of Chemistry, Materials and Chemical Engineering "Giulio Natta", Politecnico di Milano, Milan, Italy
4 Department of Pharmacy, University of Salerno, Fisciano, SA, Italy
5 Center for Omics Sciences, IRCCS San Raffaele Institute, Milano, Italy
6 ALEMBIC, Advanced Light and Electron Microscopy Bio-Imaging Center, IRCCS San Raffaele Scientific Institute, Milano, Italy.
7 Experimental Imaging Center, IRCCS San Raffaele Scientific Institute, Milano, Italy.
8 Division of Genetics and Cell Biology, IRCCS San Raffaele Scientific Institute, Milano, Italy.
9 Hepatobiliary Surgery Division, IRCCS San Raffaele Hospital, Milano, Italy.
10 Anatomical Pathology, IRCCS San Raffaele Hospital, Milano, Italy.

**These authors contributed equally*
#These authors contributed equally
^ These authors contributed equally

Corresponding authors emails: botrugno.oronzina@hsr.it; elena1.bianchi@polimi.it; tonon.giovanni@hsr.it; gabriele.dubini@polimi.it

Abstract

Patient-derived organoids (PDOs) are poised to become central tools in clinical practice, to preemptively identify patient optimal treatments, and in drug discovery, overcoming the limitations of cancer cell lines. However, the implementation of PDOs in both these settings has been hampered by several bottlenecks including sample requirements, assay time and handling in the context of high-throughput-based drug assays. We report here the development of a microfluidic-based device (Microfluidic Platform for Organoids culture, MPO) that miniaturises and greatly simplifies PDO cultures in a 384-plate format. Both retrospective and prospective clinical studies demonstrate its predictive value and the swift and straightforward implementation in the clinical setting. Obtaining comprehensive functional and molecular information on the response to drugs is becoming a requirement in drug discovery. MPO allows subcellular phenotypic and imaging screenings, target engagement for the assessment of the efficacy of therapies, alongside the ability to comprehensively and concomitantly define PDOs genomic, transcriptomic, proteomic, lipidomic and metabolomic landscape. In all, we demonstrate the potential of our platform to impact clinical practice generating relevant information on drug sensitivity within a time frame that could inform treatment decisions alongside exploration of the mechanisms underlying compound response and resistance in drug discovery efforts.

Introduction

Knowing preemptively which therapy may benefit a specific cancer patient represents the most daunting unmet clinical need in oncology. Solving this challenge will provide patients immediate relief from the disease and prevent unwanted toxicities, often severe in the case of cancer therapies. Insofar, the selection of the most appropriate treatment has been largely confined to targeted therapies, relying on the genomic analysis of patient-derived samples. In fact, the availability of therapies directly targeting cancer cells endowed with specific genetic lesions has provided remarkable successes, exemplified by mutations in EGFR in non–small cell lung cancer, BRAF in melanoma, and TRK in various cancer types[1]. However, several large prospective clinical trials[2–5], most prominently the NCI-MATCH trial[6,7], have demonstrated a limited response rate in an intention-to-treat analysis for these genomic-based therapies, not reaching 5% of all cases[1].

One potential and enticing opportunity to overcome this sobering clinical reality is the combination of static genomic measurements with the direct testing of large arrays of compounds directly on patient-derived samples, before administering any treatment, that is, the functional precision medicine (FPM) paradigm[1,8]. FPM efforts have been proposed several decades ago, whereby attempts have been made to assess the response to treatment directly on patient derived samples. These efforts have been hampered by several technological barriers, including rudimentary *ex vivo* culture methods and low-throughput capabilities, and thus they never entered clinical practice[9].

Recent technological breakthroughs have in large part tackled these roadblocks[10]. In particular, the PDOs, stem-cell derived self-organized 3D models, closely mimic *in vitro* the complex structure and function of the corresponding

healthy or diseased *in vivo* tissue, including cellular heterogeneity, histopathological features and genomic profiles of the corresponding tumour of origin[11]. They can be derived and quickly expanded from the tissues of patients and stored in "living biobanks"[12]. In the last decade, PDOs have become a central tool for therapeutic screening and precision medicine especially in the cancer field[13–16], overcoming the limitations of standard two-dimensional (2D) cell cultures and even patients derived xenografts (PDX)[10,17]. Cells grown in monolayer, the primary model for drug screening, are easy and practical but do not reproduce the complexity of a tumour tissue in terms of cellular heterogeneity, gene expression profiles, pathways activity and drug sensitivity[18]. When compared with PDXs, PDOs are easier to work with, less time-consuming, more efficient, less expensive and amenable to high-throughput drug screenings[10]. Notably, a tight correlation between patient and PDOs responses to drugs has been firmly established in several tumour types[14,16,19,20], further supporting the role of PDOs as patient avatars that could predict response to therapy[10]. These and other studies have demonstrated the feasibility of medium-throughput drug screenings on PDOs, mostly used as retrospective models or to inform patients about second line treatments or adjuvant therapies.

One of the major challenges and still unmet goals for organoid research is to use PDOs as prospective models for defining the optimal treatments for cancer patients. Crucial for the effectiveness of this approach is the development of innovative systems to perform high-throughput drug screens that reduce the time between PDO derivation and testing, within a frame that could inform clinical treatment decisions. Miniaturisation can increase the capability of existing bioassays. However, when applied to 3D models as organoids there are constraints that limit their use in high-throughput applications, such as the incorporation of multiple cell

types, the heterogeneity in size, volume and density, and the embedding in ECM to support 3D architecture[21]. The manipulation of the most commonly used extracellular matrix substitutes for organoids culturing[22] is challenging due to their non-Newtonian rheology and thermosensitive behaviour[23]. These characteristics limit their compatibility with the liquid-handling robots commonly used in HTS assays, which are designed to fill 384 and 1,536 well plates. Additionally, cell distribution homogeneity and reproducible cell seeding, key parameters for robust HTS-based approaches[24], are challenging when seeding small multicellular structures as organoids, particularly prone to sedimentation. Several culturing systems have been described that try to overcome limitations imposed by ECM embedding. In these protocols, suspensions of organoids in medium containing a small percentage of ECM are dispensed by liquid-handling robots onto the microwell plates coated with the preferred matrix on top of which organoids grow[25–28]. These procedures, while rendering organoids culture more practical for HTS-based assays, present limitations that do not fully recapitulate the best organoids culturing conditions and are only suitable for short term assays.

Other technological advancements pertain to the field of microfluidics, which has now reached a level of maturity whereby the simultaneous high-throughput screening of hundreds of compounds and combinations on patient samples is within reach[10]. In this scenario, 3D-microfluidic culture systems might offer a rapid and cost-effective solution to the aforementioned needs through advanced strategies for cell seeding, compartmentalization, continuous flow, mechanical and biochemical stimuli administration, and single-cell analyses [29–32].

Efforts are ongoing to complement traditional functional assays of cell viability, such as those based on intracellular enzyme activity or ATP, with methods that

faithfully assess the cellular phenotypes emerging from exposure to drugs [33–37]. As a matter of fact, oftentimes effective therapeutic compounds do not elicit extensive cell death, nor select for genetic subclones, but exert more subtle and yet impactful dynamic phenotypic responses.

Another major challenge for potential treatment guidance is the development of robust readouts that integrate drug response features with proteogenomic profiling of PDOs[38–40]. For such a readout, instruments are required to enable the recovery and handling of individual samples, preserving their integrity. Traditional microfluidics is based on irreversibly sealed microchips, where constructs have to be labour-intensively seeded and harvested through microchannels[41]. A recent trend shows a new generation of openable/resealable systems that on one side simplify the handling of biological samples but on the other increase the technical complexity of the system operations[42,43].

Here, we propose a microfluidic based-device (MPO) to miniaturise organoids culture in ECM. Extensive validation of the platform has been performed by exploiting a biobank of genomically and clinically annotated PDOs generated from tissue resections of colorectal cancers liver metastasis (mCRC) exposed to combinations of drugs reproducing the chemotherapeutic regimens used for treating this condition. The platform allows integrative multi-omics analysis and high-content imaging studies in PDOs-based HTS applications. The reduction in the reagents needed to perform drug screening enabled the determination of basic response parameters within a few weeks of organoids derivation.

Results

MPO allows the concomitant seeding and culturing of hundreds of PDOs

We have developed a platform based on a microfluidic approach, Microfluidic Platform for Organoids culture (MPO) which enables high-throughput seeding, culturing in a miniaturized format and drug testing of PDOs. MPO combines some basic microfluidic strategies and 3D printing approaches with the standards of a laboratory of cell biology (see Materials and Methods). MPO includes a custom dispenser, named BMdrop (Biological Matrices drop dispenser)(Fig.1A) that allows the rapid and automated seeding of organoids embedded in extracellular matrices. Microsamples of organoids are seeded in 3D printed custom structures named NESTs (Fig.1A). These structures allow the immobilization of the organoids in single 3D culture units that, when dipped in the culture medium in a 384-well plate (Fig. 1B), could be preserved for extended periods of time (Fig. 1C). Moreover, this configuration enables the handling of each 3D culture unit as a single sample in downstream applications as proteo-genomic and high-content imaging-based assays.

MPO in the clinical setting

The pre-emptive identification of the optimal treatment remains the crucial unmet clinical need in oncology. The time required to obtain PDOs from patient samples still remains a critical issue for the implementation of PDO technology in the clinical arena[10]. For example, in the SENSOR trial, the average time for development of PDOs from metastatic colon cancer samples was 10 weeks[44]. We hence designed

a prospective clinical study whose primary goal was the definition of the time needed after surgery to obtain and test PDOs in the MPO. We surmised that the small amount of material required by the MPO may shorten the time needed to obtain these data. The study lasted 18 months from April 2023 to October 2024, a total of 66 tumour samples were collected from 61 patients undergoing surgical resections of metastatic colo-rectal cancer to the liver (mCRC) and from whom 37 PDOs were derived. The success rate of tumour PDOs generation was highly dependent on the quality and size of resections, proportion of cancer cells and cell proliferation rate, as previously reported[10,14,16,44,45]. For 26 PDOs out of 37 the average time to establish enough organoids for performing an initial drug testing was less than 4 weeks, with several integrated into the platform and screened as early as one week after surgery (Supplementary Fig. 1A).

We also sought to determine the predictive value of the MPO. To properly address this question, we first had to define the threshold discriminating between sensitive versus resistant PDOs. To this end, we added to the prospective study PDOs a second retrospective cohort, for a total of 52 PDOs, exposed to treatment in the MPO for 96h, when drug effects were quantified (Fig. 2A). PDOs were seeded into the platform and exposed to a combination of drugs reproducing two chemotherapeutic regimens commonly used as first-line treatments for patients with mCRC, namely FOLFOX (FOX) and FOLFIRI (FIRI)[46]. In order to maintain patient-relevant concentrations, each chemotherapeutic combination was used at two concentrations, the maximum clinically achievable plasma concentration (Cmax) reported for each drug (FOX2 and FIRI2)[47–50] and 10-fold lower (FOX1 and FIRI1). This strategy ensured the exposure of PDOs at a range of drug concentrations that are relevant to those observed in the clinical practice[51]. Independent assays

demonstrated the robustness and reproducibility of the MPO (Supplementary Fig. 2 and 3), also when compared with the conventional 96-well microplate setting (Supplementary Fig. 4). Clustering based on the sensitivity to lower concentrations separated PDOs into sensitive or resistant, with the threshold distinguishing the two groups set at 40% viability relative to the untreated control (Fig. 2A, Supplementary Fig. 2 and 3). Of note, most of the PDOs were either sensitive or resistant to both treatments although there were two exceptions: PDO#63 which was more sensitive to FOLFIRI and PDO#163, which was more sensitive to FOLFOX (Fig. 2A, Supplementary Fig. 2 and 3).

We hence relied on this threshold to determine the predictive value of MPO in a subset of patients exposed to postoperative adjuvant chemotherapy. These patients were treated with combinations of 5-FU and oxaliplatin or 5-FU and irinotecan regimens (Supplementary Fig. 1B). In a 24-months follow-up study, we observed a significant correlation between *in vitro* PDOs response and disease free survival (DFS)(Fig. 2B), with a median DFS of 24 and 7 months in patients from whom sensitive and resistant PDOs were respectively derived (Fig. 2B and Supplementary Fig. 1B).

These data suggest robust predictive capabilities of the MPO for FOLFOX and FOLFIRI chemotherapy and emphasise the strong potential of the MPO as a tool for anticipating clinical responses to a vast array of drugs thus guiding treatment decisions.

High-content imaging of PDOs cultured in MPO

Imaging-based screening methods generate accurate measurements of multiple cellular features across conditions allowing phenotypic analyses, efficacy

studies, and target localization, providing crucial information on cellular states and transitions arising from treatments. As such, this approach is relevant both for assessing the clinical response to drugs, and in HTS to obtain more reliable information on compound effects[35]. We hence tested whether imaging-based approaches could be applied also to MPO. Mindful of the challenges that cells grown on a 3D system may broach for reliable collection of images, when compared with cells on 2D systems[52], we modified the grid architecture, elongating the NEST support, to position the surface of the matrix embedding PDOs closer to the bottom of the wells, to reduce the working distance and allow the visualisation of the PDOs by confocal microscopy (Supplementary Fig. 5A).

We next assayed quantitative immunofluorescence. To this end, we confirmed the staining of phosphorylated HA2X, a proxy of DNA damage[53], on untreated PDOs, as well its nuclear staining after exposure of the PDOs grown within MPO to standard chemotherapies (Fig. 3A and B and Supplementary Fig. 5B). Phalloidin staining of actin filaments confirmed that the treatment did not affect the overall morphological features of the PDOs (Fig. 3A), while FOLFIRI treatment resulted in an increase in the nuclear area of both PDOs (Fig. 3C).

We then determined if we could exploit MPO for 3D live-imaging. We engineered MCF7 cells, expressing a fluorescently tagged NF-kB mScarlet-p65[54]. We grew these cells as spheroids and transferred them to MPO. Similarly to what is observed in 2D cell cultures[54], after stimulation with the NF-KB activator TNFα, we were able to detect the shuttling of mScarlet-p65 from the cytoplasm to the nucleus as early as 1 hour after stimulation (Fig. 3D and Supplementary Fig. 5C). Importantly, MPO also allows single cell tracking. We adapted our image analysis protocols[55] to track single cells and quantify the activation of p65 by measuring the

ratio of the nuclear to cytosolic mScarlet-p65 intensity (Fig. 3E and F) over time both in untreated and treated cells.

We next explored whether we could harness other imaging methods not requiring the use of antibodies, nor relying on previous assumptions, to explore the response of cells to the exposure to compounds or to genetic manipulation. Cell Painting has emerged as one of the most prominent unbiased, quantitative, high-dimensional profiling techniques, leveraging on six fluorescent dyes to comprehensively describe eight subcellular components or organelles, including nuclei (Hoechst 33342 Nuclear stain), nucleoli (Nucleic Acid staining), cytoskeleton (Phalloidin), mitochondria (Mitochondrial Stain), Endoplasmic Reticulum (Concanavalin A), and the Golgi apparatus (Wheat Germ Agglutinin [WGA])[52,56]. We adjusted the 2D Cell Painting protocol to stain and image the 3D structures directly embedded in matrices (see Materials and Methods). We were able to identify in the PDOs grown in MPO all the subcellular organelles usually detected by Cell Painting (Supplementary Fig. 5D). We attempted also to visualize the entire 3D structures, reconstructing the spatial organization of the PDOs, with the representation of the subcellular compartments and the relationships between them (Supplementary Fig. 5E).

In all, these results demonstrate that MPO is amenable to multiparameter imaging-based phenotypic profiling that complements traditional functional assays to provide a complete picture of cellular events that may reveal hidden vulnerabilities triggered by exposure to drugs.

Genomic and transcriptomic definition of PDOs cultured in the MPO

Despite the limitations listed above, the definition of the genetic lesions affecting a cancer, and the identification of mutated or translocated proteins, remain the mainstay of personalized medicine. Importantly, several reports have highlighted how mutated genes are not necessarily expressed in the corresponding cancer cells[57–60], suggesting that it is imperative to determine not only the mutational status of a gene, but also whether it is expressed, to guide the selection of the most appropriate targeted therapies to administer to patients. We thus sought to define both the genetic landscape and the expression profiles of the PDOs grown in the MPO. To obtain from the same PDOs both DNA and mRNA information, we selected and adapted the G&T-seq protocol[61], which provides parallel sequencing of genomic DNA and mRNA. Low-pass whole genome sequencing (WGS) of PDOs grown and treated into the MPO revealed a high degree of overlap of the copy number variants (CNV) profiles between untreated PDOs grown on the platform and on those derived from a 24-well plate (Fig. 4A). In line with the known distinction of colorectal cancer patients, PDO#62, a microsatellite instable tumor (MSI) showed minimal if any copy number variations, while PDO#74 and PDO#61, microsatellite stable (MSS), showed chromosomal rearrangements (Fig. 4A). Conversely, an RNA-seq analysis performed on several PDOs demonstrated how PDOs clustered together, at baseline and after treatments (Fig. 4B).

When we explored the concordance between the genetic mutational status and the RNA levels of the corresponding genes in three PDOs, we found a strong concordance between these two set of information in each PDO (Fig. 4C),

suggesting indeed that the G&T could provide crucial information on the expression level of mutated genes, to guide treatment decisions.

Target engagement assessment of drug response of PDOs treated in the MPO

Determining whether a drug is engaging with its target is pivotal in both addressing the efficacy of a treatment in a specific patient, as well as in drug discovery to define the spectrum of activity of compounds[62–64]. We hence explored whether it is possible to measure target engagement also in the MPO miniaturized setting. To this end, we adapted to the MPO the HTRF (Homogeneous Time Resolved Fluorescence)-based protocol[65], which combines fluorescence resonance energy transfer technology (FRET) with time-resolved measurement (TR) MPO (Supplementary Fig. 6A). We selected PDOs presenting mutations in the KRAS gene, and exposed them to the pan KRAS inhibitor BI-2865[66]. To assess target engagement, we assayed the phosphorylation status of ERK, a direct target of RAS, alongside ERK total levels (Fig. 5). HTRF adapted to MPO demonstrated that BI-2865 strongly inhibited ERK phosphorylation in the treated samples without affecting ERK total levels. In parallel, we also asked whether BI-2865 was able to inhibit other kinases, namely AKT, whose activity is under the control of RAS in some cellular settings. BI-2865 indeed mildly decreased pAKT levels, without impacting on AKT total levels. In parallel, we assessed the activity of the specific PIK3CA inhibitor alpelisib[67]. As expected, alpelisib did not suppress ERK signalling but reduced AKT phosphorylation (Fig. 5), without any effect on the total protein levels of ERK and AKT. A conventional western blot analysis of the same PDOs grown and treated in

standard assay conditions confirmed MAPK and PI3K pathways modulation (Supplementary Fig. 7A and B) as seen in HTRF-based assays.

In all, these results demonstrate how MPO could be used for high-throughput measurements of target engagement.

High-throughput proteomic, metabolomic and lipidomic analyses on PDOs treated in the MPO

It is becoming increasingly evident that a thorough assessment of the activity of a compound entails a comprehensive understanding not only of the genomic and transcriptomic modifications induced by a drug, but importantly refined measurements of the proteome, the metabolome and the lipidome profiles[68–70]. The main obstacle to the widespread adoption of these analyses rests on the requirement for mass spectrometry-based approaches of sizable amounts of starting material. We hence explored whether PDOs grown within the MPO could be leveraged for these analyses.

We first asked whether the few microliters of PDOs present in each NESTpillar may provide enough material to perform proteomic, metabolomics and lipidomics analyses. To this end, we performed a simultaneous MS-based multiomic profiling. Notably, for each NEST pillar we obtained an average of 1,200 proteins, 32 polar metabolites and 123 lipids (data not shown).

We next explored whether proteomic analysis might provide insights on the response of PDOs to treatment. We exposed one PDO (#61) to the chemotherapy regimens described above. We retrieved 2,061 proteins as differentially expressed between samples (0.1% FDR). PCA and clustering including all samples revealed that treated and non-treated samples were neatly separated. Intriguingly, samples treated with either FOLFOX or FOLFIRI at high dosage clustered together, while samples exposed to lower concentrations for each regimen were separated in the PCA (Fig. 6A). We thus embarked to define the set of proteins altered by high dosage exposure. To this end, 379 proteins were collectively modulated by the higher drug concentration, with 56 proteins in common between the two treatments. By performing STRING interaction enrichment (Fig. 6B), we found that the top 6

KEGG pathways ranked by strength of interaction were Mismatch repair, spliceosome, Arginine and Proline metabolism, RNA transport, Glutathione metabolism and central carbon metabolism in cancer (Fig. 6C).

We next explored which proteomic changes were instead induced by the exposure of PDOs to low dosages. The proteins emerging as differentially present between controls and lower FOLFIRI concentration included proteins belonging to intracellular membrane-bounded organelle, serine biosynthesis and NAD metabolism (Supplementary figure 8A-D). In this context, key targets involved in serine biosynthesis such as PSAT1 and PHGDH were identified and found generally reduced in the FOLFIRI treated group. Additionally, other key proteins such as Aldehyde dehydrogenases ALDH1B1 were part of the network. In the case of FOLFOX at low doses, central carbon metabolism in cancer, RNA transport and negative mRNA regulation of metabolic processes related proteins were affected (Supplementary figure 8E-H).

As for the lipidomic analysis, we were able to annotate and quantify 123 lipids belonging to 11 lipid subclasses. Treatments reduced all lipid classes detected, independently from the concentration (Fig. 7), with FOLFOX reducing lipid biosynthesis more than FOLFIRI. We then performed an in-silico functional lipidomics analysis to evaluate potential routes of lipid biosynthesis hampered by each treatment. FOLFOX treatment appeared to halt the synthesis of phosphatidylcholines (PCs) from lysophosphatidylcholines (LPCs) and phosphatidylinositols (PIs). This effect may stem from an indirect influence on phospholipase A2 (PLA2), which plays a crucial role in PC remodeling. Consequently, the inhibition of PLA2 activity could reduce PC turnover and limit its recycling into signaling molecules (Supplementary Figure 9a). When considering lipid building blocks, we noticed an overall extension of fatty acid chain length from C16 to C18, coupled with the inhibition of monounsaturated C18:1 fatty acid biosynthesis, that suggests alterations in the activity of key enzymes involved in fatty acid elongation (ELOVL) and desaturation (SCD). On the other hand, FOLFIRI treatment affected the conversion of phosphatidylethanolamine (PEs) to PCs (SupplementaryFigure 9b). Overall the lipidomics profiling suggests a membrane lipid breakdown as result of oxidative damage and more broadly a stress-adaptive mechanism to cope with chemotherapy treatment.

Polar metabolome profiling resulted in 32 metabolites annotated with MSI level = 2 or =1 when an authentic standard was available. While this number is low it should be underlined that within the same pillar, three different biomolecules were simultaneously extracted, which is challenging for the very low volume and cell number available. Nevertheless, important metabolites such as lactate, succinate, choline, serine, different acylcarnitines and free fatty acids were profiled. Their trend with the treatment is reported in the hierarchical clustering reported in Supplementary figure 10, which indicates that FOLFOX and FOLFIRI elicit a different metabolome perturbation.

In all, these results demonstrate that the MPO, combining drug sensitivity assays performed on PDOs with proteomic studies, allows for better ex vivo modelling of drug responses. This underscores the potential of the MPO to more effectively uncover individual tumour vulnerabilities and to predict tumour response to therapeutic agents.

Discussion

We propose an innovative microfluidic platform that allows the high-throughput screening of PDOs, overcoming several of the limitations that insofar have hampered the introduction of the PDO technology both in the clinical practice and in drug discovery. While the standard practice for 3D cell culture privileges lab handwork and 48 or 96-plate format culturing[71–73], we designed and validated a system that combines 3D printing, microfluidics, and biological lab standards to build a fast, affordable, versatile, and robust drug screening platform on PDOs in 384-plate.

There are several key features of the MPO, which we propose as innovative, including the seeding of organoids already embedded in ECM, the use of 3D printed biocompatible material for 3D culture and the straightforward integration of MPO into

laboratory standards. This approach hence greatly simplifies the execution of survival, phenotypic and omic screenings, as well as of high-content imaging. Specifically, the NESTs culture setting, allowing a swift replacement of the culture medium and retrieval of the PDOs, overcomes limitations that restrict the scalability towards HTS by most of the emerging devices in microfluidic and organ-on-a-chip field. It targets a standardisation of the method, as advocated by the Focus Group Organ-on-Chip Standardization Roadmap CEN/CENELEC FGOoC. The design strategy tailored around 3D printing allows a fast scalability (even of NEST microstructures) to afford HTS and a wide pre-clinical research validation. The seeding process, as a result of the combination of BMdrop and NESTs, overcomes a current limitation of the standard in bioprinting Matrigel, directly delivering organoids embedded in Matrigel, and distributing them homogeneously among the NESTs culture units. BMdrop and NESTs are optimized are designed to be tunable to fit different protocols, as they could be utilized with different dilutions or grades of ECM, different drop volumes, and include different populations or densities of cells. The dispenser BMdrop is then a compact and low-complexity instrumentation, provided by Standard Operation Procedures documentation. All these conditions pave the way for a possible use in both small or well-equipped laboratories and to support the introduction of PDOs into the clinical practice.

All together, these novel approaches herald a new, preemptive, “try-it-all” era that promises to deliver more effective and less toxic treatments for cancer patients[74]. Indeed, alongside several ongoing studies based on FPM[1,10], a few functional clinical trials have already been implemented with remarkable successes[1,75], even obtaining exceptional responses in heavily pretreated patients (EXALT trial; [76]). Other studies are ushering new enticing paths, integrating ex-vivo

screenings (as for the FPM paradigm) alongside extensive, in depth, multi-omic tumor profiling and clinical data, to predict patient responses[77,78].

In the clinical trial setting, the dosing and schedule of treatments is almost always empirical, hampering efforts to test and validate more innovative therapeutic schemes such as adaptive and metronomic approaches. Additionally, identifying the most effective combination therapy in the clinical setting is challenging. A large study involving over 1,000 PDX has revealed that fewer than 5% of combinations improved progression-free survival more effectively than the best monotherapy[79]. While the success of combination therapies in cancer treatment has been well-documented[80], much of this success has been attributed to the “bet-hedging” paradigm of independent drug action[81], which posits that a single drug within a combination is primarily responsible for cancer cell killing in each specific patient. Beside bet-hedging, the potential of synthetic lethal and additive or synergistic drug combinations has also been firmly established in the clinic[82]. Examples include the use of PARP inhibitors in BRCA-mutated cancers, the combination of BRAF and EGFR inhibitors in *BRAF*-mutant colon cancer and collateral lethality through co-deletions[83] or co-amplifications[84]. While many promising combinations have been identified *in vitro*, their clinical translation has been hampered by two primary factors: reliance on inadequately predictive preclinical models[17] – and the dependency on overly sensitive cell lines that inflate the perceived impact of additivity or synergistic interactions[81]. MPO is poised to address these critical medical needs, identifying the most effective compounds, at the proper concentration, maximizing efficacy while preventing unnecessary toxicities. Specifically for targeted therapies, MPO allows to gauge target engagement across a broader concentration range beyond the commonly used IC50[85], addressing the so-called Drug-Dosing Conundrum in

Oncology[86] and aligning with initiatives like the FDA Project Optimus. More broadly, in the setting of phase I and phase II clinical trials, the availability of multi-layered data from each PDOs will assist towards the definition of biologically efficacious dose (BED), leveraging on "effect markers"[85].

The introduction of targeted therapies has heralded a new era in cancer treatment, but also posed new challenges. For cytotoxic therapies, the maximum tolerated dose (MTD), while variable across patients, has nonetheless provided a useful benchmark to define the dose to be used during the clinical trial phase and then in the clinical practice. Targeted therapies often do not exhibit dose limiting doses. Thus, the MTD is often difficult to attain and may not guide the definition of the dose to be implemented in the clinic[85]. Various strategies have been implemented, which include target-mediated drug disposition (TMDD), with the clearance of the drug used as a proxy; measurements of downstream effects, again prone to approximations, such as IL2 levels in the bloodstream over a 2,000-fold dose range of Pembrolizumab, and others. In all, these methods provide only an approximation of the optimal dose to be used and often correspond to an incomplete target engagement, with suboptimal responses[81]. Therefore, with these therapies, for the single patient, undertreatment is very frequent, but at times also overtreatment, leading to toxicity-driven early discontinuation, where lower doses could instead be highly effective[81]. Measuring the impact of a targeted compound directly on its target could provide a robust, reliable, assessment of its effectiveness on the tumour of a specific patient.

Phenotypic screenings are enticing, as they are poised to provide critical and complementary information to conventional genomic assessments (ref Letai). Unbiased approaches such as Cell Painting seem to be especially apt to high-

throughput screenings as they do not require extensive sample processing nor of course preemptive knowledge of proteins and targets to be assessed with specific antibodies. However, obtaining reliable images for high-throughput phenotypic screenings from 3D structures like PDOs has proven challenging[52]. We demonstrate that the Cell Painting protocol could be adapted to PDOs, obtaining selective stainings without evident differences from the existing findings. We should note that as reported in 2D cultures[52], we detected some cytoplasmic staining visible in the RNA channel, and the ER channel shows noticeable nucleolar staining while staining of the other compartments was specific for the expected targeted cellular organelle/compartments. Among the challenges that we encountered, the most prominent were the obstacles to dye penetration inside the dense 3D structures and the matrigel.

We envision that tools like MPO might exert a major impact both in the clinical practice by generating relevant information on drug sensitivity in a time frame that could inform treatment decisions, as well as in the drug discovery programs driven by the pharma industry and academia, to define the mechanisms of action of drug libraries.

Acknowledgements

We wish to thank all the members of the Tonon, Dubini, Campiglia, Mazza, Zambrano, Tacchetti and Cittaro labs for helpful discussions and suggestions, alongside the clinical colleagues of the Aldrighetti team. This work was supported by the Accelerator Award: A26815 entitled: ‘Single-cell cancer evolution in the clinic’ funded through a partnership between Cancer Research UK and Fondazione Italiana per la Ricerca Sul Cancro (AIRC)(to GT and GD); the Italian Ministry of Health grant (RF-2021–12374586)(to GT); the italian Ministry of Education, University and

Research, project PNC0000001 D34 Health—Digital Driven Diagnostics, prognostics and therapeutics for sustainable Health care “CUP” B53C22006090001 to G.T., P. C. and C.T.; the Italian Ministry of Education, University and Research, project PRIN - “Microfluidic Platform for Cancer Drug Screening - MicroCaDS”, project funded by the European Union - Next Generation EU, Mission 4, Component 1, “CUP” D53D23003310006 (to G.D and G.T.); the MUSA - Multilayered Urban Sustainability Action – project, funded by the European Union – NextGenerationEU, under the National Recovery and Resilience Plan (NRRP) Mission 4 Component 2 Investment (to. G.D). Line 1.5: strengthening research structures and creation of R&D “innovation ecosystems”, set up of “territorial leaders in R&D” (to PC); Project “Pathogen Readiness Platform for CERIC ERIC upgrade”—PRP@CERIC CUP J97G22000400006, to P. C.; Project National Center for Gene Therapy and Drugs based on RNA Technology CUP: D43C22001200001, to P. C.

Figure legends

Figure 1. Description of the MPO. A. The “BMdrop dispenser” includes a pump, to dispense controlled volumes of samples, connected to a custom-made cartridge. Organoids resuspended in PBS are mixed to the biological matrix and the resulting solution is preloaded into the cartridge equipped with an iced core to prevent gelation. The pump allows the extrusion of microfluidic drops of the organoids suspension then seeded into individual nests organized in grids. **B.** Grids are overturned and positioned in a 384-well plate, where each nest is dipped in the culture medium of a single well. The panel on the left shows a grid with the NESTs filled with the suspension of organoids before the culture; in the middle panel, the grid is positioned inside the plate; the right panel shows a 384-well plate filled with 8 grids for a total of 288 single NESTs. **C-D.** a PDO was cultured in the MPO and viability evaluated at different timepoints by CellTiter-Glo assay (C) and bright-field imaging analysis (D). Cell viability is reported as Relative Luminescence Units (R.L.U.). The culture was stopped at day 25 when no further increase in the R.L.U. values were observed. One representative of three independent experiments is shown.

Figure 2. Drug sensitivity test of organoids grown and treated in the platform.

A. A panel of 52 PDOs lines were seeded in the 3D culture platform and exposed to a combination of drugs that replicated two chemotherapeutic regimens commonly used to treat patients with mCRC. Two concentrations were used, one highest (FOX2 and FIRI2) based on the Cmax reported for each drug and one 10–fold lower (FOX1 and FIRI1). The heatmap summarizes the sensitivities to the chemotherapeutic combination regimens reported as the mean percentage of viable cells in treated relative to untreated control samples averaged from a minimum of two independent experiments, each performed in six technical replicates per condition. The range of responses among the different organoids allowed their separation into two major groups: sensitive and resistant. **B.** A Kaplan-Meier curve of disease-free survival for patients eligible for adjuvant chemotherapy and whose organoids were reported as sensitive or resistant. Gehan-Breslow-Wilcoxon and Log-rank (Mantel-Cox) tests were used to determine statistical significance among the two groups of patients. The exact P is shown based on both tests.

Figure 3. Quantitative imaging of living and fixed 3D cell structures cultured and stained in the 3D platform. A. Hoechst, Phalloidin, and γH2AX staining of PDO#6 and PDO#17 left untreated (NT) or treated with FOLFIRI (FIRI). **B-C**. Quantification of γH2AX nuclear intensity (B) and nuclear area (C) of NT and FIRI-treated organoids. **D.** Spheroids of MCF7 cells expressing mScarlet-p65 were stained with Hoechst and either left untreated (NT) or treated with TNFα (panels on the left). On the right, snapshots of the time lapse images representative of NT and TNFα-treated spheroids under constant stimulation. **E.** Representative single-cell profiles of nuclear to cytosolic m-Scarlet-p65 intensity for NT and TNFα-treated spheroids. **F.** Area under the curve (AUC) of the nuclear to cytosolic mScarlet-p65 intensity profiles quantified for cells in NT and TNFα-treated spheroids.

Figure 4. 3D culture platform enables integration of multiple genomics platforms. A. Manhattan plot of the Read Depth (RD) signal for WGS of PDO#61, PDO#62 and PDO#74 on the 3D platform (left) and on the 24-well plate (right). Copy number variations (CNVs) are conserved across technologies. **B.** Principal component analysis (PCA) of the RNA-seq data, each dot represents one sample, x-axis, principal component 1, represents 31% of variance; y-axis, principal component

2, represents 23% of variance. Samples are grouped by organoid, with distinct clusters within each PDO representing the time of drug administration and treatment. **C.** Degree of concordance between RNA and DNA among three PDOs.

Figure 5. Target engagement by HTRF-based assays on organoids grown and treated on the 3D culture platform.

A panel of 4 $KRAS_{mut}$ PDOs lines were seeded in the 3D culture platform and treated for 4 hours either with DMSO (NT) or BI-2865 (KRASi) or Alpelisib. Levels of phospho-ERK (pERK), phospho-AKT (pAKT), total ERK and AKT were assessed in HRTF-based assays. Results are reported as the levels of each protein in the treated samples relative to the untreated counterpart (ratio/NT) averaged (± standard error of the mean [SEM]) from three independent experiments, each performed in six technical replicates per condition. A two-way ANOVA followed by Sidak's multiple comparisons test was used to determine statistical significance between groups. . *P<0.05 ** P<0.01; *** P<0.001; **** P<0.0001.

Figure 6. Proteomics, analysis on organoids grown and treated on the 3D culture platform.

A. Principal component analysis score plot relative to PDO#61 reporting the clustering of different treatments. **B.** String protein-protein interaction network with highlighted nodes for **C**. KEGG pathway enrichment relative to highlighted nodes.

Figure 7. Untargeted Lipidomics analysis on organoids grown and treated on the 3D culture platform.

Normalized concentration of lipid subclasses and their trend in PDO#61: NT (black bar), FOLFOX (green bar), FOLFIRI (pink bar). Lipid abbreviations: Cholesterol esters (CE), Ceramides (CERs), Sphinogmielyns (SMs), Lysophosphatidylcholines (LPCs), Phosphatidilcholines (PCs), Ether-linked Phosphatidilcholines (PC-Os), Phosphatidylethanolamines (PEs), Ether-linked Phosphatidilcholines (PE-Ps), Phosphatidylinositols (PIs), Triacylglycerols (TGs), Ether-linked triacylglycerol (TG-Os).

Supplementary Figures

Supplementary Figure 1. Retrospective and prospective drug sensitivity test of organoids grown and treated on the 3D culture platform.

A. The table summarizes the PDOs lines used in the prospective study and week after the explant at which they were subjected to the first screen. **B.** The table shows the correlation between the response data of the organoids (sensitivity and resistance as reported in Figure 2) and the clinical outcome, measured as disease-free survival, of the corresponding patients. The median disease-free survival of both groups is shown.

Supplementary Figure 2. Retrospective drug sensitivity test of organoids grown and treated on the MPO.

A panel of 26 PDOs lines were seeded in the platform and exposed to a combination of drugs that reproduced two chemotherapeutic regimens commonly used to treat patients with mCRC. Two concentrations were used, one highest (FOX2 and FIRI2) based on the Cmax reported for each drug and one 10–fold lower (FOX1 and FIRI1). For each PDO line, at least three independent experiments were performed in six technical replicates for each condition. In the case of PDO#67, experiments were two. Red boxes indicate the PDOs derived from patients eligible for adjuvant chemotherapy. **A.** For each condition, results are presented as the mean percentage (± standard error of the mean [SEM]) of viable cells in treated relative to untreated control (NT) samples averaged from independent experiments. **B.** For each experiment, results are presented as the mean percentage (± standard deviation [SD]) of viable cells in treated relative to untreated control (NT) samples averaged from six technical replicates.

Supplementary Figure 3. Prospective drug sensitivity test of organoids grown and treated on the MPO.

A panel of 26 PDOs lines were seeded in the platform and exposed to a combination of drugs as reported for the retrospective study. At least two independent experiments are reported for each PDOs line, all performed within one month from surgical resection. The red box indicates a PDO line derived from a patient eligible

for adjuvant chemotherapy. **A.** For each condition, results are presented as the mean percentage (± standard error of the mean [SEM]) of viable cells in treated relative to untreated control (NT) samples averaged from independent experiments. **B.** For each experiment, results are presented as the mean percentage (± standard deviation [SD]) of viable cells in treated relative to untreated control (NT) samples averaged from six technical replicates.

Supplementary Figure 4. Comparison between drug sensitivity tests performed in conventional 96-well microplate setting or on the MPO.

Three PDOs lines were seeded in a conventional 96-well microplate setting or in the MPO and exposed to a combination of drugs as reported for the retrospective study. For each condition, results are calculated as the mean percentage (± standard deviation) of viable cells in treated relative to untreated control samples (NT) averaged from a minimum of three (in the 96-well microplate) or six technical repetitions. In each panel, the mean (± SEM) of three independent experiments is reported for each PDOs line. A two-way ANOVA followed by Sidak's multiple comparisons test was used to determine statistical significance between groups.

Supplementary Figure 5. Representative movies of living and fixed 3D cell structures cultured and stained in the 3D platform.

A. For imaging purposes, the NESTs grid architecture was modified to position the surface of the matrix embedding the PDOs closer to the bottom of the wells. **B.** Optical sectioning (left) and 3D reconstruction (right) of immunofluorescence of a representative PDO stained for Hoechst, phalloidin and γH2AX. **C.** Time-lapse of an optical section of an untreated (NT, top) and TNFα-treated (bottom) spheroid derived from MCF7 cells expressing mScarlet-p65 and stained with Hoechst. Individual channels and the merged channels are shown. **D-E.** Representative image of Cell Painting staining of PDO#17. Single channels show respectively: cyan – nuclei, green – endoplasmic reticulum, grey – RNA and nucleolus, red – cytoskeleton, yellow – Golgi apparatus, magenta – mitochondria. In line with a previous report [52], some cytoplasmic staining is noticeable in the RNA channel and the nucleolar staining appears in the E.R. channel. 2D projected single images (D) and 3D color composite image as a volumetric reconstruction (E) of the organoid.

Supplementary Figure 6. Target engagement by HTRF-based assays on organoids grown and treated on the 3D culture platform.

A. Schematic representation of the experimental procedure for the HTRF-based assays in the 3D culture platform. **B.** The ratio between control lysate signal relative to non-specific signal for each assay. Results are averaged (± standard error of the mean [SEM]) from three independent experiments, each performed in three technical replicates per condition.

Supplementary Figure 6. Western Blot analysis of PDOs lines treated with BI-2865 and Alpelisib.

A. Western blot analysis for the expression of the indicated proteins was performed on the same PDOs lines grown and treated as in Fig. 3 but not in a miniaturized setting. Vinculin was used as loading control. One representative experiment of two is shown. **B.** Quantification of the bands of the western blot assay presented in A.

Supplementary Figure 8.

Proteomics analysis of PDO#61 showing PCA, heatmap and enrichment for significant proteins at low and high dosage for FOLFIRI (A-D) and FOLFOX (E-H) treatments

Supplementary Figure 9. Functional lipidomics analysis of FOLFOX and FOLFIRI treated PDOs.

Functional lipidomics analysis of FOLFOX (A) and FOLFIRI (B) treated PDO#61 reporting modulated lipid biosynthesis routes obtained by in-silico comparisons.

Supplementary Figure 10. Hierarichical clustering of untargeted metabolomics analysis of FOLFOX and FOLFIRI treated PDO#61.

References

1. Letai, A., Bhola, P. & Welm, A. L. Functional precision oncology: Testing tumors with drugs to identify vulnerabilities and novel combinations. *Cancer Cell* **40**, 26–35 (2022).
2. Middleton, G. *et al.* The National Lung Matrix Trial of personalized therapy in lung cancer. *Nature* **583**, 807–812 (2020).
3. Le Tourneau, C. *et al.* Molecularly targeted therapy based on tumour molecular profiling versus conventional therapy for advanced cancer (SHIVA): a multicentre, open-label, proof-of-concept, randomised, controlled phase 2 trial. *The Lancet Oncology* **16**, 1324–1334 (2015).

4. Chen, A. P. *et al.* Molecular Profiling-Based Assignment of Cancer Therapy (NCI-MPACT): A Randomized Multicenter Phase II Trial. *JCO Precision Oncology* (2021) doi:10.1200/PO.20.00372.
5. Tilburg, C. M. van *et al.* The Pediatric Precision Oncology INFORM Registry: Clinical Outcome and Benefit for Patients with Very High-Evidence Targets. *Cancer Discov* **11**, 2764–2779 (2021).
6. Flaherty, K. T. *et al.* Molecular Landscape and Actionable Alterations in a Genomically Guided Cancer Clinical Trial: National Cancer Institute Molecular Analysis for Therapy Choice (NCI-MATCH). *Journal of Clinical Oncology* (2020) doi:10.1200/JCO.19.03010.
7. O'Dwyer, P. J. *et al.* The NCI-MATCH trial: lessons for precision oncology. *Nat Med* **29**, 1349–1357 (2023).
8. Letai, A. Functional Precision Medicine: Putting Drugs on Patient Cancer Cells and Seeing What Happens. *Cancer Discovery* **12**, 290–292 (2022).
9. Letai, A. Functional precision cancer medicine-moving beyond pure genomics. *Nature Medicine* **23**, 1028–1035 (2017).
10. van Renterghem, A. W. J., van de Haar, J. & Voest, E. E. Functional precision oncology using patient-derived assays: bridging genotype and phenotype. *Nat Rev Clin Oncol* **20**, 305–317 (2023).
11. Clevers, H. Review Modeling Development and Disease with Organoids. *Cell* **165**, 1586–1597 (2016).
12. Schutgens, F. & Clevers, H. Human Organoids: Tools for Understanding Biology and Treating Diseases. *Annu. Rev. Pathol. Mech. Dis.* **15**, 211–234 (2020).
13. Barroso, M. *et al.* A path to translation: How 3D patient tumor avatars enable next generation precision oncology. *Cancer Cell* **40**, 1448–1453 (2022).
14. Ooft, S. N. *et al.* Patient-derived organoids can predict response to chemotherapy in metastatic colorectal cancer patients. *Science Translational Medicine* **11**, 1–10 (2019).
15. Tuveson, D. & Clevers, H. Cancer modeling meets human organoid technology. *Science* **364**, 952–955 (2019).
16. Vlachogiannis, G. *et al.* Patient-derived organoids model treatment response of metastatic gastrointestinal cancers. *Science* **359**, 920–926 (2018).
17. Honkala, A., Malhotra, S. V., Kummar, S. & Junttila, M. R. Harnessing the predictive power of preclinical models for oncology drug development. *Nat Rev Drug Discov* **21**, 99–114 (2022).
18. Loewa, A., Feng, J. J. & Hedtrich, S. Human disease models in drug development. *Nat Rev Bioeng* 1–15 (2023) doi:10.1038/s44222-023-00063-3.
19. Weeber, F. *et al.* Preserved genetic diversity in organoids cultured from biopsies of human colorectal cancer metastases. *Proc. Natl. Acad. Sci. U.S.A.* **112**, 13308–13311 (2015).
20. Tiriac, H. *et al.* Organoid profiling identifies common responders to chemotherapy in pancreatic cancer. *Cancer Discovery* **8**, 1112–1129 (2018).
21. De Stefano, P. *et al.* Bioprinting of Matrigel Scaffolds for Cancer Research.

Polymers **13**, 2026 (2021).
22. LeSavage, B. L., Suhar, R. A., Broguiere, N., Lutolf, M. P. & Heilshorn, S. C. Next-generation cancer organoids. *Nat. Mater.* **21**, 143–159 (2022).
23. Kane, K. I. W. *et al.* Determination of the rheological properties of Matrigel for optimum seeding conditions in microfluidic cell cultures. *AIP Advances* **8**, 125332 (2018).
24. Iversen, P. W. *et al.* HTS Assay Validation. in *Assay Guidance Manual* (eds. Markossian, S. et al.) (Eli Lilly & Company and the National Center for Advancing Translational Sciences, Bethesda (MD), 2004).
25. Sachs, N. *et al.* A Living Biobank of Breast Cancer Organoids Captures Disease Heterogeneity. *Cell* **172**, 373-386.e10 (2018).
26. van de Wetering, M. *et al.* Prospective Derivation of a Living Organoid Biobank of Colorectal Cancer Patients. *Cell* **161**, 933–945 (2015).
27. Brandenberg, N. *et al.* High-throughput automated organoid culture via stem-cell aggregation in microcavity arrays. *Nat Biomed Eng* **4**, 863–874 (2020).
28. Verissimo, C. S. *et al.* Targeting mutant RAS in patient-derived colorectal cancer organoids by combinatorial drug screening. *eLife* **5**, e18489 (2016).
29. Badr-Eldin, S. M., Aldawsari, H. M., Kotta, S., Deb, P. K. & Venugopala, K. N. Three-Dimensional In Vitro Cell Culture Models for Efficient Drug Discovery: Progress So Far and Future Prospects. *Pharmaceuticals* **15**, 926 (2022).
30. Eduati, F. *et al.* Patient□specific logic models of signaling pathways from screenings on cancer biopsies to prioritize personalized combination therapies. *Molecular Systems Biology* **16**, e8664 (2020).
31. El-Ali, J., Sorger, P. K. & Jensen, K. F. Cells on chips. *Nature* **442**, 403–411 (2006).
32. De Stefano, P., Bianchi, E. & Dubini, G. The impact of microfluidics in high-throughput drug-screening applications. *Biomicrofluidics* **16**, 031501 (2022).
33. Rafelski, S. M. & Theriot, J. A. Establishing a conceptual framework for holistic cell states and state transitions. *Cell* **187**, 2633–2651 (2024).
34. Moshkov, N. *et al.* Predicting compound activity from phenotypic profiles and chemical structures. *Nat Commun* **14**, 1967 (2023).
35. Chandrasekaran, S. N., Ceulemans, H., Boyd, J. D. & Carpenter, A. E. Image-based profiling for drug discovery: due for a machine-learning upgrade? *Nat Rev Drug Discov* **20**, 145–159 (2021).
36. Berg, E. L. The future of phenotypic drug discovery. *Cell Chemical Biology* **28**, 424–430 (2021).
37. Kang, J. *et al.* Improving drug discovery with high-content phenotypic screens by systematic selection of reporter cell lines. *Nat Biotechnol* **34**, 70–77 (2016).
38. Savage, S. R. *et al.* Pan-cancer proteogenomics expands the landscape of therapeutic targets. *Cell* **187**, 4389-4407.e15 (2024).
39. Ji, S. *et al.* Pharmaco-proteogenomic characterization of liver cancer organoids for precision oncology. *Sci. Transl. Med.* **15**, eadg3358 (2023).
40. Mani, D. R. *et al.* Cancer proteogenomics: current impact and future prospects. *Nat Rev Cancer* **22**, 298–313 (2022).

41. Teixeira Carvalho, D. J., Moroni, L. & Giselbrecht, S. Clamping strategies for organ-on-a-chip devices. *Nat Rev Mater* **8**, 147–164 (2023).
42. Virumbrales-Muñoz, M. *et al.* Enabling cell recovery from 3D cell culture microfluidic devices for tumour microenvironment biomarker profiling. *Sci Rep* **9**, 6199 (2019).
43. Schuster, B. *et al.* Automated microfluidic platform for dynamic and combinatorial drug screening of tumor organoids. *Nat Commun* **11**, 5271 (2020).
44. Ooft, S. N. *et al.* Prospective experimental treatment of colorectal cancer patients based on organoid drug responses. *ESMO Open* **6**, 100103 (2021).
45. Veninga, V. & Voest, E. E. Tumor organoids: Opportunities and challenges to guide precision medicine. *Cancer Cell* **39**, 1190–1201 (2021).
46. Van Cutsem, E. *et al.* ESMO consensus guidelines for the management of patients with metastatic colorectal cancer. *Annals of Oncology* **27**, 1386–1422 (2016).
47. Satoh, T. *et al.* Pharmacokinetic assessment of irinotecan, SN-38, and SN-38-glucuronide: a substudy of the FIRIS study. *Anticancer Res* **33**, 3845–3853 (2013).
48. Chabot, G. G. Clinical pharmacokinetics of irinotecan. *Clin Pharmacokinet* **33**, 245–259 (1997).
49. Graham, M. A. *et al.* Clinical pharmacokinetics of oxaliplatin: a critical review. *Clin Cancer Res* **6**, 1205–1218 (2000).
50. Bocci, G. *et al.* Comparative pharmacokinetic analysis of 5-fluorouracil and its major metabolite 5-fluoro-5,6-dihydrouracil after conventional and reduced test dose in cancer patients. *Clin Cancer Res* **6**, 3032–3037 (2000).
51. Liston, D. R. & Davis, M. Clinically Relevant Concentrations of Anticancer Drugs: A Guide for Nonclinical Studies. *Clinical Cancer Research* **23**, 3489–3498 (2017).
52. Bray, M.-A. *et al.* Cell Painting, a high-content image-based assay for morphological profiling using multiplexed fluorescent dyes. *Nat Protoc* **11**, 1757–1774 (2016).
53. Rogakou, E. P., Pilch, D. R., Orr, A. H., Ivanova, V. S. & Bonner, W. M. DNA Double-stranded Breaks Induce Histone H2AX Phosphorylation on Serine 139. *Journal of Biological Chemistry* **273**, 5858–5868 (1998).
54. Zambrano, S., De Toma, I., Piffer, A., Bianchi, M. E. & Agresti, A. NF-κB oscillations translate into functionally related patterns of gene expression. *eLife* **5**, e09100 (2016).
55. Kizilirmak, C. *et al.* Small transcriptional differences among cell clones lead to distinct NF-κB dynamics. *iScience* **26**, 108573 (2023).
56. Fredin Haslum, J. *et al.* Cell Painting-based bioactivity prediction boosts high-throughput screening hit-rates and compound diversity. *Nat Commun* **15**, 3470 (2024).
57. Ma, X. *et al.* Pan-cancer genome and transcriptome analyses of 1,699 paediatric leukaemias and solid tumours. *Nature* **555**, 371–376 (2018).
58. Rashid, N. U. *et al.* Differential and limited expression of mutant alleles in

multiple myeloma. *Blood* **124**, 3110–3117 (2014).
59. Govindan, R. *et al.* Genomic landscape of non-small cell lung cancer in smokers and never-smokers. *Cell* **150**, 1121–34 (2012).
60. Shah, S. P. *et al.* The clonal and mutational evolution spectrum of primary triple-negative breast cancers. *Nature* **486**, 395–9 (2012).
61. Macaulay, I. C. *et al.* G&T-seq: Parallel sequencing of single-cell genomes and transcriptomes. *Nature Methods* **12**, 519–522 (2015).
62. Waring, M. J. *et al.* An analysis of the attrition of drug candidates from four major pharmaceutical companies. *Nat Rev Drug Discov* **14**, 475–486 (2015).
63. Cook, D. *et al.* Lessons learned from the fate of AstraZeneca's drug pipeline: a five-dimensional framework. *Nat Rev Drug Discov* **13**, 419–431 (2014).
64. Bunnage, M. E., Chekler, E. L. P. & Jones, L. H. Target validation using chemical probes. *Nat Chem Biol* **9**, 195–199 (2013).
65. Degorce, F. HTRF: A Technology Tailored for Drug Discovery - A Review of Theoretical Aspects and Recent Applications. *TOCHGENJ* **3**, 22–32 (2009).
66. Kim, D. *et al.* Pan-KRAS inhibitor disables oncogenic signalling and tumour growth. *Nature* **619**, 160–166 (2023).
67. Fritsch, C. *et al.* Characterization of the Novel and Specific PI3Kα Inhibitor NVP-BYL719 and Development of the Patient Stratification Strategy for Clinical Trials. *Molecular Cancer Therapeutics* **13**, 1117–1129 (2014).
68. Wenk, M. R. The emerging field of lipidomics. *Nat Rev Drug Discov* **4**, 594–610 (2005).
69. Wishart, D. S. Emerging applications of metabolomics in drug discovery and precision medicine. *Nat Rev Drug Discov* **15**, 473–484 (2016).
70. Meissner, F., Geddes-McAlister, J., Mann, M. & Bantscheff, M. The emerging role of mass spectrometry-based proteomics in drug discovery. *Nat Rev Drug Discov* **21**, 637–654 (2022).
71. Laborde, N. *et al.* Human colonic organoids for understanding early events of familial adenomatous polyposis pathogenesis. *The Journal of Pathology* **265**, 26–40 (2025).
72. Esposito, A. *et al.* Colorectal cancer patients-derived immunity-organoid platform unveils cancer-specific tissue markers associated with immunotherapy resistance. *Cell Death Dis* **15**, 1–12 (2024).
73. Zhong, Z. *et al.* Human immune organoids to decode B cell response in healthy donors and patients with lymphoma. *Nat. Mater.* 1–15 (2024) doi:10.1038/s41563-024-02037-1.
74. Dolgin, E. The future of precision cancer therapy might be to try everything. *Nature* **626**, 470–473 (2024).
75. Malani, D. *et al.* Implementing a Functional Precision Medicine Tumor Board for Acute Myeloid Leukemia. *Cancer Discov* **12**, 388–401 (2022).
76. Kornauth, C. *et al.* Functional Precision Medicine Provides Clinical Benefit in Advanced Aggressive Hematologic Cancers and Identifies Exceptional Responders. *Cancer Discovery* **12**, 372–387 (2022).
77. Bottomly, D. *et al.* Integrative analysis of drug response and clinical outcome

in acute myeloid leukemia. *Cancer Cell* **40**, 850-864.e9 (2022).
78. Irmisch, A. *et al.* The Tumor Profiler Study: integrated, multi-omic, functional tumor profiling for clinical decision support. *Cancer Cell* **39**, 288–293 (2021).
79. Gao, H. *et al.* High-throughput screening using patient-derived tumor xenografts to predict clinical trial drug response. *Nature Medicine* **21**, 1318–1325 (2015).
80. Jin, H., Wang, L. & Bernards, R. Rational combinations of targeted cancer therapies: background, advances and challenges. *Nat Rev Drug Discov* **22**, 213–234 (2023).
81. Plana, D., Palmer, A. C. & Sorger, P. K. Independent Drug Action in Combination Therapy: Implications for Precision Oncology. *Cancer Discovery* **12**, 606–624 (2022).
82. Doroshow, J. H. & Simon, R. M. On the Design of Combination Cancer Therapy. *Cell* **171**, 1476–1478 (2017).
83. Muller, F. L., Aquilanti, E. A. & DePinho, R. A. Collateral Lethality: A New Therapeutic Strategy in Oncology. *Trends in Cancer* **1**, 161–173 (2015).
84. Bei, Y. *et al.* Passenger Gene Coamplifications Create Collateral Therapeutic Vulnerabilities in Cancer. *Cancer Discovery* **14**, 492–507 (2024).
85. Sachs, J. R., Mayawala, K., Gadamsetty, S., Kang, S. P. & De Alwis, D. P. Optimal Dosing for Targeted Therapies in Oncology: Drug Development Cases Leading by Example. *Clinical Cancer Research* **22**, 1318–1324 (2016).
86. Shah, M., Rahman, A., Theoret, M. R. & Pazdur, R. The Drug-Dosing Conundrum in Oncology — When Less Is More. *N Engl J Med* **385**, 1445–1447 (2021).
87. Potenza, A. *et al.* Revealing and harnessing CD39 for the treatment of colorectal cancer and liver metastases by engineered T cells. *Gut* gutjnl-2022-328042 (2023) doi:10.1136/gutjnl-2022-328042.
88. Yao, Y. *et al.* Patient-Derived Organoids Predict Chemoradiation Responses of Locally Advanced Rectal Cancer. *Cell Stem Cell* **26**, 17-26.e6 (2020).
89. Stringer, C., Wang, T., Michaelos, M. & Pachitariu, M. Cellpose: a generalist algorithm for cellular segmentation. *Nat Methods* **18**, 100–106 (2021).
90. Angermueller, C. *et al.* Parallel single-cell sequencing links transcriptional and epigenetic heterogeneity. *Nature Methods* **13**, 229–232 (2016).
91. Li, H. Aligning sequence reads, clone sequences and assembly contigs with BWA-MEM. *arXiv* **1303.3997v2**, (2013).
92. Dobin, A. *et al.* STAR: Ultrafast universal RNA-seq aligner. *Bioinformatics* **29**, 15–21 (2013).
93. Suvakov, M., Panda, A., Diesh, C., Holmes, I. & Abyzov, A. CNVpytor: a tool for copy number variation detection and analysis from read depth and allele imbalance in whole-genome sequencing. *GigaScience* **10**, giab074 (2021).
94. Danecek, P. *et al.* Twelve years of SAMtools and BCFtools. *GigaScience* **10**, giab008 (2021).

Material and methods

Microfluidic Platform for Organoids culture MPO

The MPO consists of two main parts: the “BMdrop dispenser”, includes a pump and a custom-made cartridge to deliver PDOs embedded in matrices directly into the 6x6 NESTs grids. They are then placed in culture in a 384-well plate (Corning® Flat Clear Bottom White Polystyrene), each NEST in a well. The cartridge consists of a polymeric tubing specifically arranged in a cooled shell, to prevent the gelation and the sedimentation of the suspension of organoids in biological matrices. Each cartridge can store the 650 µL of the sample (PBS+ Matrigel® + PDOs) to seed 72 NESTs (two grids). The NEST is a 3D printed structure (Formlab, Form 3B+, Biomed Resin, SLA Stereolithography), designed to accommodate 8 µL of the sample inside a pseudo-cylindrical cavity, defined by eight pins and open top. In the culture configuration the NEST is hung, overturned and immersed in the 384-well plate, the 3D culture sample in the NEST is exposed to cell culture media through the open side and the spaces between pins. The cartridge is connected to a syringe pump (PhD2000 Harvard Apparatus) that drives the dispensing of single drops of homogeneous PDOs suspension to single NESTs in a fast, reliable way, as characterized in our previous work. Cartridges are individually packaged, sterilized, and autoclaved. Each set of NESTs is washed three times in DI ultrapure water, dried, and then sterilized in UV under the biological hood.

Human tissue samples.

All procedures were approved by the Institutional Review Board of IRCCS San Raffaele Scientific Institute and were compliant with all relevant ethical regulations. Patient samples were collected at the Clinical Department at San Raffaele Hospital (Milan, Italy) under written informed consent in agreement with the Declaration of Helsinki (Protocol “ACC_ORG”, Milan, Italy). All data were stored according to best practices, protecting patient confidentiality and data integrity.

Patient-derived CRC-LM organoids generation.

Patient-derived organoids (PDOs) were obtained essentially as already reported[87]. Briefly, surgical resections of LM-CRC were minced, and digested in 5mM

PBS/EDTA supplemented with 2X TrypLe (Gibco, A1217701) and 500U recombinant DNase I (Roche, 04716728001) at 37°C for 60 min. Cells released in the solution were resuspended in growth factor reduced Matrigel® (Corning, 356231) and seeded in a 24-well flat bottom cell culture plate (Corning). After solidification, Matrigel® domes were overlaid with Advanced DMEM/F12 (Gibco, 12634028) supplemented with 1X B27 (Gibco,17504044), 1X N2 (Gibco, 17502048), 1% penicillin-streptomycin (Euroclone, ECB3001D), 1% glutamine (Gibco, 25030081), 1% BSA (Sigma-Aldrich, 10735086001) and with the following growth factors: 50 ng/mL EGF (PeproTech, 100-39H), 100 ng/mL Noggin (PeproTech, 250-38), 500 ng/mL R-Spondin 1 (PeproTech, 120-38), 10 nM gastrin (Sigma-Aldrich, G9145), 10 ng/mL FGF-10 (PeproTech, 100-26), 10 ng/mL FGF-basic (PeproTech, 100-18B), 100 ng/mL Wnt-3A (R&D Systems, 5036-WN), 1 µM prostaglandin E2 (Tocris Bioscience, 2296), 10 µM Y-27632 (StemCell Technologies, 72304), 4 mM nicotinamide (Sigma-Aldrich, N0636), 0,5 µM A83-01 (Tocris Bioscience, 2939), 5 µM SB202190 (Sigma-Aldrich, S7067). Medium was changed every 2–3 days.

Seeding and culturing of PDOs in the MPO

Sub-confluent PDOs were harvested, mechanically and enzymatically dissociated into single cells by incubating with TrypLE select enzyme and replated[87]. Cells were allowed to generate small PDOs for 2-3 days and then recovered with the Cell Recovery solution (Corning, 354253). Recovered PDOs were diluted in a solution composed of 50% Matrigel® or Cultrex Basement Membrane Extract (R&D Systems, 3432-010-01) in PBS. The suspension of PDOs was then loaded into the BMdrop dispenser and organoids were seeded onto the NESTs grids and cultured as described above. For the long-term culture, PDOs were plated in the MPO and maintained in culture for up to 25 days. Medium was refreshed every 3-4 days by placing NESTs grids in a new 384-well plate with fresh medium. Growth of organoids was evaluated at fixed points analysing organoid viability by CellTiter-Glo assay and bright-field imaging analysis. The culture was stopped when no further increase in the luminescence values was observed, indicating that the culture had reached a balance between cell viability and death.

Drug screening

Oxaliplatin and 5-FU were obtained from the pharmacy at San Raffaele Hospital and dissolved in PBS. SN-38, the active metabolite of irinotecan (Sellekchem, S4908),

was dissolved in DMSO (Sigma-Aldrich, D8418). Compounds were kept at stock concentrations of 1000X in the vehicle. Before treatments, drugs were further diluted to 1X final concentration in complete PDO medium and 70 µL of this solution were added in each well. DMSO or PBS treated PDOs served as control. DMSO concentration in the medium was 0.1%. For the retrospective and prospective studies PDOs were seeded in the platform and exposed to two chemotherapeutic combinations, both used at two concentrations: FOX1: 40 µM 5-FU and 1.25 µM Oxaliplatin

FOX2: 400 µM 5-FU and 12.5 µM Oxaliplatin

FIRI1: 40 µM 5-FU and 10 nM SN-38

FIRI2: 400 µM 5-FU and 100 nM SN-38

Organoids were incubated with the compounds at 37°C for 96 hours with no further changes of media or compounds refresh. After treatment PDOs were displaced from the chip into a new empty 384-well white plate (Corning, by centrifugation (3 minutes at 800 x g). Cell viability was quantified by a 1:1 mix of CellTiter-Glo 3D (Promega, G9681) and Advanced DMEM/F12, according to the manufacturer's instructions and incubated for 45 min at RT. The luminescence signal was measured on a Mithras LB 940 microplate reader (Berthold Technologies). Drug screenings were repeated at least twice and treatments performed in six technical replicates. In the prospective study, the optimal time for drug screening was defined based on the organoids growth rate and size (50-100 µm)[88]. Mean of the luminescence values of the six technical replicates was calculated for each condition and reported as percentage of viable cells relative to the untreated samples. Then, mean ± Standard Error of the Mean (S.E.M.) between biological independent experiments was calculated.

PDOs imaging and data analysis

For immunofluorescence staining, PDOs were plated on NESTs grid supports specifically designed for imaging applications and exposed to drugs as described above. After treatment, PDOs were stained directly into the NESTs grid. All steps were performed at room temperature and solutions were prepared in PBS. PDOs were fixed in a solution of 4% paraformaldehyde (Electron Microscopy Sciences, 157-8) and 2% sucrose (Sigma-Aldrich, S0389) for 30 minutes and then permeabilized with 0.1% Triton X-100 (Sigma-Aldrich, T8787) for 8 minutes. Nonspecific antigens were blocked in a solution of 5% BSA (Sigma-Aldrich, A8022) and 10% goat serum (Sigma-Aldrich, G9023) for 30 minutes, and then PDOs were

incubated with monoclonal antibody γH2AX (Biolegend, 613402) at 1:200 dilution in 2.5% BSA for 4 hours. After incubation for 2 hours with a solution of goat anti-mouse IgG Alexa Fluor™ 488 (Invitrogen, A-11001) at 1:500, 10µg/mL Hoechst 33342 (Invitrogen, H3570) and 4µg/mL rhodamine phalloidin (Invitrogen, R415) in 2. 5% BSA, the NESTs grid was placed on a new empty 384-well black glass bottom microplate (Ibidi, 88407) and PDOs were centrifuged at 400g for 3 minutes to collect the individual drops within the wells. Drops were overlaid with PBS, the microplate sealed with an optical adhesive film (TermoFisher, 4311971) and stored at 4°C prior to imaging. 16 bit -1024x1024 pixels images were acquired using a 60X silicone immersion objective on an Olympus Fluoview 3000RS (Olympus Life Sciences) confocal microscope. Nuclei were manually segmented in ImageJ (The Mathworks Inc.) to estimate nuclear area and the average fluorescence intensity per nucleus in the γH2AX channel was evaluated. Statistical test: Bonferroni corrected Kolmorogov-Smirnov test.

Spheroids culture live imaging and data analysis

MCF7 stably expressing p65-mScarlet construct, were generated by lentiviral infection. Federica Colombo and Alessandra Agresti kindly shared plasmids and protocol for p65-mScarlet lentiviral infection and HEK-293T cells were used for virus production. Infected MCF7 cells were sorted for high mScarlet signal and NF-kB activation upon TNFα was validated via confocal imaging following the previously described procedure for live cell imaging in 2D[54]. To allow spheroid formation, mScarlet-p65 MCF7 single cells were plated on uncoated low-attachment dishes with a density of 300 cells/cm^2 and cultured for 5 days. Before imaging, spheroids were embedded in Matrigel and plated in the NESTs, treated with 20 ng/ml TNF or vehicle control and live imaged using Olympus Fluoview 3000RS confocal microscope with temperature and CO_2 control. Quantification of the evolution in time of nuclear to cytosolic intensity of p65 was performed by adapting the procedure found in [54], that can be briefly described as follows. First, nuclear and cytosolic masks of a plane of the 3D stack images were identified using CellPose[89]. Using the barycenters of the nuclei we tracked the cells using an adaptation of the Hungarian algorithm and then we calculated the background-subtracted nuclear to cytosolic average intensities for each track cell based on the nuclear and cytosolic masks. This gives values well below 1 for untreated cells and close to 1 for TNFα-treated

cells, as previously reported[54]. Area under the curve (AUC) was calculated for single nuclear to cytosolic p65 profiles of 2 hours duration.

Phenotypic profiling by Cell Painting assay

Morphological profiling using the Cell Painting jump kit (Revvity, PING21) was performed following the manufacturer's instructions and adapting a protocol previously reported[52]. PDOs were first incubated with PhenoVue 641 Mitochondrial Stain (500nM) for 1 hour at 37°C and then fixed as described above. Subsequently, PDOs were stained for PhenoVue Hoechst 33342 Nuclear Stain (1.62µM), PhenoVue Fluor 488 - Concanavalin A (48nM), PhenoVue 512 Nucleic Acid Stain (6µM), PhenoVue Fluor 555 – WGA (43.7nM), PhenoVue Fluor 568 – Phalloidin (8.25nM), in a solution of 0.1% Triton X-100 in PBS for 2 hours at room temperature. PDOs were collected onto a new empty 384-well black glass bottom microplate and stored as described above. An Olympus FLUOVIEWTM FV3000 confocal laser scanning microscope with 30X/1.05 objective was used to collect confocal z-stacks (pixel size = 0.207 µm/pixel, z-step = 1 mm) with sequential channels acquisition: laser 405 nm for Hoechst 33342, laser 488 nm for PhenoVue Fluor 488, laser 514 nm for PhenoVue 512, laser 561 nm for AlexaFluor 555, laser 594 nm for Alexa Fluor 594m and laser 640 nm for Cy5. Images were subjected to a pre-processing step of deconvolution via Huygens software. 3D reconstruction of single PDOs confocal images was performed via Arivis software (Zeiss).

Homogeneous time resolved fluorescence (HTRF)

The KRAS inhibitor BI-2865 (#HY-153724) and the PIK3CA inhibitor Alpelisib (#HY-15244) were purchased by MedChemExpress and dissolved at a 1000X concentration in DMSO. Detection of ERK and AKT expression and phosphorylation levels was performed using the total ERK (64NRKPEG), the phospho-ERK (Thr202/Tyr204) (64ERKPEG), the total AKT (64NKTPEG) and the phospho-AKT (Ser473) (64AKSPEG) cellular kits from Revvity. Organoids were seeded and grown in complete medium for 4 days. Before treatment the chip containing PDOs was placed in a 384-well plate with a minimal medium where growth factors were withdrawn, for 24 hours. After this time, the chip was placed in a new plate containing fresh minimal medium in which either DMSO or drugs were already dissolved at the final concentration (10 µM for BI-2865 and 5µM for Alpelisib).

Treatment was performed for 4 hours, then the chip was centrifuged on a 384-well plate (3 minutes at 400g) and the assay performed essentially following the manufacturer's instructions. 16 µL of 1X lysis Buffer (including 1X blocking reagent) was added to each well for 45 minutes at room temperature. After lysis, 4 µL of a 1:1 mixture of d2 and Eu Cryptate antibodies working solution was added in each well. Plates were sealed and incubated overnight at room temperature light protected. The HTRF program was used to detect signals at 620 nm and 665 nm wavelengths using a Mithras LB 940 microplate reader (Berthold Technologies, Bad Wildbad, Germany). Negative control to check the non-specific signal and positive control as provided by the manufacturer, were used in each assay. The ratio between control lysate signal/non-specific signal was greater than 2 for each assay in the 3 independent experiments performed (Supplementary Fig. 6B).

Proteomics analysis

Each organoid was subjected to a simultaneous extraction of protein, polar metabolites and lipids according to a previous protocol with minor modifications [10.1074/mcp.M115.053702]. Protein pellet digestion and clean-up was performed as reported previously{Updating}. Proteomic analysis was performed by nLC- HRMS using an Ultimate 3000 nanoLC (Thermo Fisher Scientific, Bremen, Germany) coupled to an Orbitrap Lumos tribrid mass spectrometer (Thermo Fisher Scientific) with an Easy nano electrospray ion source (Thermo Fisher Scientific). Peptides were trapped for 1 minute in a PepMap trap-Cartridge, 100 Å, 5 µm, 0.3 x 5 mm (Thermo Fisher), and separated onto a Aurora Ultimate C18 column (250 mm × 75 µm I.D, 1.7 µm, 120 , IonOpticks, Fitzroy, Australia). Mobile phases were A): 0,1% HCOOH in water v/v; B): 0,1% HCOOH in ACN/Water v/v 80/20. Peptides were separated using a linear gradient of 90 min. HRMS analysis was performed in data dependent acquisition and data independent acquisition (DDA and DIA) as follows: DDAparameters: MS1 range 400–1500 m/z, HCD fragmentation was used with normalized collision energy setting 27. Resolution was set at 120.000 for MS1 and 15.000 for MS/MS. Single charge and unassigned charge peptides were excluded. Quadrupole isolation was set to 3Da. Maximum ion injection times for MS (OT) and the MS/MS (OT) scans were set to auto and 50 ms respectively, and ACG values were set to standard. Dynamic exclusion: 30 s. For data independent acquisition (DIA) a first MS scan was performed at 120.000 resolution, DIA was performed in OT

at 15.000 resolution, with 10 Dalton isolation windows, AGC target and maximum ion injection time were set to custom using 200ms and 40 ms values, loop control was set to N=30. HCD was used with a collision energy value of 30. DDA raw MS data were analysed using Proteome Discoverer v 2.5 (Thermo Fisher), Proteins were considered identified with at least one unique peptide, using a false discovery rate (FDR) threshold of 0.1. The following parameters were used: and 0,6 Da for precursors and fragments respectively. Sequest search and Percolator algorithms were used. DIA data were analyzed with DIA-NN v 1.8 using a library free workflow, enzyme trypsin, missed cleavages max 1, mass accuracy tolerance was set to 10 ppm, Carbamidomethylcysteine was used as fixed modification while methionine oxidation as variable. Proteomics enrichment was performed with STRING: https://string-db.org/cgi/input?sessionId=beDyGfYlflHr&input_page_show_search=on

Lipids and metabolites extraction

226 µL of ice-cold methanol (MeOH) containing a blend of deuterated standards was spiked to organoid pellets kept at −30 °C for 1 minute and then transferred to an ultrasonic bath for 10 minutes. Following the addition of 750 µL of ice-cold methyl tert-butyl ether (MTBE), cells were incubated in a Thermomixer (Eppendorf) for 1 hour at 4 °C and 550 rpm. 188 µL of water (H_2O) was added to the samples, and after centrifugation, the upper (for lipids) and lower (for metabolites) layers were collected and evaporated using a SpeedVac (Savant, Thermo Scientific, Milan, Italy). Dried extracts were dissolved 150 µL of $CHCl_3$/MeOH/IPA (1/2/4) and 50 µL of H_2O/MeOH 90:10 (*v/v%*), respectively, for lipidomics and metabolomics analyses.

Lipidomics profiling

Lipidome has been profiled using a Thermo Ultimate UHPLC system (Thermo Scientific, Bremen, Germany) connected online to a TimsTOF Pro Quadrupole Time-of-Flight (Q-TOF) mass spectrometer (Bruker Daltonics, Bremen, Germany) equipped with an Apollo II electrospray ionization (ESI) source.

Lipids separation was performed using a Waters Acquity UPLC CSH™ C18 column (100 × 2.1 mm; 1.7 µm, 130 Å) paired with a VanGuard CSH™ precolumn (5.0 × 2.1 mm; 1.7 µm, 130 Å) (Waters, Milford, MA, USA). The column oven temperature was maintained at 65 °C, with a flow rate of 0.55 mL min^{-1}. The mobile

phases were composed of: (A) ACN/H_2O 60:40 (*v/v %*) and (B) IPA/ACN 90:10 (*v/v %*), both buffered with 10 mM $HCOONH_4$ and 0.1% HCOOH (*v/v %*) for the positive ionization mode and with 10 mM CH_3COONH_4 and 0.1% CH_3COOH (*v/v %*) for the negative ionization mode. The following gradient was applied: 0 min, 40% B; 0.4 min, 43% B; 0.425 min, 50% B; 0.9 min, 57% B; 2.0 min, 70% B; 2.950 min, 99% B; 3.3 min, 99% B; 3.31 min, 40% B, followed by a 0.7 min re-equilibration of the column.

At the start of each run, mass and mobility accuracy were recalibrated by injecting a mixture (1:1 *v/v %*) of 10 mM sodium formate calibrant solution and ESI-L Low Concentration Tuning Mix. Data-dependent parallel accumulation serial fragmentation (DDA-PASEF) acquisition mode was employed. Both positive and negative ESI ionization were used in separate runs, with each sample analyzed in duplicate. The injection volume was set at 2 µL and 3 µL, respectively, for positive and negative ionization mode. ESI source parameters were set as follows: nebulizer gas (N_2) pressure at 4.0 bar, dry gas (N_2) flow rate at 10 L/min, and dry temperature at 280 °C. Mass spectra were collected over the m/z range of 50–1500, with accumulation and ramp times of 100 ms each. Ion mobility was scanned from 0.55 to 1.80 Vs/cm². Precursors were isolated within ± 2 m/z and fragmented using ion mobility-dependent collision energies MS/MS stepping mode: 1/K0 [Vs/cm²] 0.55-1.8; CE [eV] #1: 20–40 and CE [eV] #2: 35–50. The total acquisition cycle lasted 0.32 seconds, consisting of one PASEF ramp. Exclusion time was set to 0.1 minutes, and ion charge control (ICC) was configured to 7.5 million.

Data alignment, filtering, and annotation were carried out using MetaboScape 2023b (Bruker) that uses a feature-detection algorithm (T-Rex 4D). The feature detection threshold was set to 250 counts for both positive and negative ionization modes, with a minimum of 75 data points in the 4D-TIMS space. Lipidomics data were deconvoluted in positive mode using $[M+H]^+$, $[M+Na]^+$, $[M+K]^+$, $[M+H–H_2O]^+$ and $[M+NH_4]^+$ ions, and in negative mode using $[M−H]^-$, $[M+Cl]^-$, $[M+CH_3COO]^-$ and $[M−H_2O]^-$ ions. Lipids were annotated through a rule-based approach and the LipidBlast spectral library in MS-DIAL. Molecular formulas were assigned using SmartFormula™ (SF). Compound annotation has been performed setting the following parameters: mass accuracy (narrow: 2 ppm, wide: 10 ppm), mSigma (narrow: 30, wide: 250), MS/MS score (narrow: 800, wide: 150), and Collision Cross-

Section (CCS) % (narrow: 2, wide: 3.5). CCS values were compared with predictions from the CCSbase platform.

After the annotation process, all spectra were manually curated and examined. Manual curation of each lipid was then performed following Lipidomics Standard Initiative (LSI) guidelines (https://lipidomics-standards-initiative.org/guidelines/lipid-species-identification/general-rules), specifically, besides MS/MS diagnostic ions, crucial aspects of lipid annotation such as (a) lipid adducts in electrospray ionization and (b) regular retention behavior, e.g., the equivalent carbon number (ECN) model used for RPLC, were carefully evaluated. LipidCreator tool (https://lifs-tools.org/lipidcreator.html) extension in Skyline (https://skyline.ms/project/home/begin.view) was used for in silico comparison of specific product ions. Lipids missing in more than 75% of real samples and 50% of QC samples were excluded. Additionally, lipids with a Coefficient of Variation (CV) above 30% among QCs were discarded. Lipid intensities were normalized using the corresponding deuterated internal standard. The dataset was then log-transformed and autoscaled for multivariate data analysis. Functional lipidomics analysis was performed with LipidOne: https://lipidone.eu/

Metabolomics profiling

Metabolome analyses were performed on a Thermo Vanquish Neo UHPLC (2.1 mm I.D setup) coupled online to a hybrid quadrupole Orbitrap Exploris 120 mass spectrometer (Thermo Fisher Scientific, Bremen, Germany) equipped with a heated electrospray ionization probe (HESI II). The MS was daily calibrated by Pierce™ FlexMix™ calibration solutions in both polarities. Metabolites separation was performed with an Acquity UPLC HSS T3™ (150 × 1.0 mm; 1.8 µm, 100Å), the column temperature was set at 55 °C, a flow rate of 100 µL/min was used, mobile phase consisted of (A): H_2O + 0.1% HCOOH and (B): ACN + 0.1% HCOOH were used for positive ionization, while 0.1% CH_3COOH was used for negative ionization mode. The following gradient has been used: 0 min, 0% B; 6 min, 70% B; 8 min, 80% B; 9 min, 98% B, 10 min 98% B; 10.1 min 0% B and 3.9 min for column re-equilibration. The HESI source parameters for 1.0 mm i.d setup were: sheath gas 20 a.u, auxiliary gas 7 a.u, sweep gas 0. Spray voltages were set to 3.3 kV and 3.0 kV for ESI (+) and ESI (-) respectively, Ion transfer tube and vaporizer temperature were set to 280° and 150°C respectively, in both RP and HILIC modes. MS data

acquisition for both setups was performed in full scan-data dependent acquisition (FS-DDA) in the m/z 70-800, MS1 resolution was set to 60000, the AGC target was set to auto with a maximum injection time at 100 ms. MS/MS was employed with an isolation window of 1-5 Da, dynamic exclusion of 10s, resolution was set to 15.000, and HCD was used with normalized collision energies of 20, 40 and 60. The instrument was externally calibrated daily with FlexMix solution (ThermoFisher) while at the beginning of every LC run the internal calibrant was injected (IC run start mode). FreeStyle (Thermo Fisher Scientific) was used to visualize RAW data, which were then imported to Compound Discoverer v.3.3 (Thermo Fisher Scientific) to normalize, align, detect and identify compounds. Features were extracted from 0-10 min and 0-11 min of the HILIC and RP chromatography runs, respectively, in the m/z= 70-800 mass range. Data were aligned according to an adaptive curve alignment model. Compounds were detected using the following parameters settings: mass tolerance was set to 5 ppm, while retention time tolerance was set to 0.2 min; minimum peak intensity was set to 100000 AU and the signal-to-noise threshold for compound detection was set to 5. The peak rating filter was set to 3. To perform blank subtraction, we maintained max sample/max blank ratio > 5. For statistical comparison between the two setup, signal intensity was normalized by using the algorithm “Constant Sum”. To predict elemental compositions of the compounds, the relative intensity tolerance was set to 30% for isotope pattern matching. For the mzCloud database search, both the precursor and fragment mass tolerance were set to 5 ppm. The databases used for matching compounds in ChemSpider for structural search were BioCyc, the Human Metabolome Database and KEGG, and the mass tolerance in ChemSpider Search was set to 5 ppm. The mass tolerance for matching compounds in Metabolika pathways was set to 5 ppm. Compounds were assigned by comparing annotations using the following nodes in order of priority: (1) mzCloud (2) Predicted Compositions; (3) MassList search; (4) ChemSpider Search; (5) Metabolika search.

MS-multi-omics data analysis

Data analysis was conducted using MATLAB (The MathWorks, Inc., Natick, MA, USA) with custom-written scripts and standard MATLAB functions. The workflow

encompassed data preprocessing, univariate and multivariate statistical analysis, and visualization.

The filtered data were normalized using the Probabilistic Quotient Normalization (PQN) [https://doi.org/10.1021/ac051632c] method. The median spectrum of the dataset was used as the reference for normalization to ensure comparability across samples and mitigate variability arising from experimental conditions.

An Analysis of variance (ANOVA) [Wackerly, Dennis D. "Mathematical Statistics with Applications 7th ed." (2008); Dunn, Olive Jean, and Virginia A. Clark. Applied statistics: analysis of variance and regression. John Wiley & Sons, Inc., 1986] with False Discovery Rate (FDR) [https://doi.org/10.1111%2Fj.2517-6161.1995.tb02031.x] correction was performed to identify statistically significant variables. This approach minimized the likelihood of false positives, ensuring the robustness of the findings.

The variables identified as significant from the ANOVA analysis were used to generate heatmaps. Data for the heatmaps were further normalized by rows to enhance interpretability and emphasize relative differences within each variable across samples.

Successively, the normalised data were preprocessed prior to multivariate analysis to ensure comparability and enhance interpretability. All variables were transformed using a base-10 logarithmic transformation to scale the distribution and reduce the impact of large variations. Following the logarithmic transformation, the data were autoscaled by centering each variable to a mean of zero and scaling to a variance of one. This preprocessing step ensures that all variables contribute equally to the analysis, irrespective of their original scales and units.

Principal Component Analysis (PCA) was employed as an unsupervised multivariate exploratory technique to reduce dimensionality and identify patterns or clusters within the data. PCA projects the original data into a new coordinate system, defined by orthogonal axes called principal components (PCs), which are linear combinations of the original variables. The first principal component captures the greatest variance in the data, while subsequent components account for decreasing amounts of variance, under the constraint of orthogonality.

The PCA results are summarized in terms of scores and loadings. While the scores represent the projections of samples onto PCs, effectively describing the position of each sample in the reduced dimensional space, in order to identify trends, clusters,

or outliers among the samples; the Loadings represent the contributions of the original variables to each principal component, providing insight into which variables drive the observed patterns in the scores. High absolute values of loadings indicate variables with significant influence on the corresponding component.

The scores plot included confidence ellipses calculated based on the Hotelling's (T2) statistic, a multivariate generalization of variance. The T2 statistic provides a measure of the distance of each sample from the center of the scores distribution within the PCA space. Confidence ellipses were calculated at the 98% confidence level, representing the region where 98% of the samples are expected to fall, assuming multivariate normality. Samples outside the confidence ellipse are considered potential outliers, which may warrant further investigation

Immunoblots and antibodies

Whole-cell extracts were obtained by lysis in sodium dodecyl sulphate (SDS) buffer (50 mM of Tris HCl pH 6.8, 10% glycerol, 2% SDS). Proteins were separated by SDS-polyacrylamide gel electrophoresis, blotted onto an Nitrocellulose membrane (Merck KGaA, Darmstadt, Germany), and probed with the indicated antibodies. Clarity Western ECL Blotting Substrate (Bio-Rad, Hercules, CA, USA) was used for the chemiluminescent reaction. The antibodies used were as follow: Phospho-Akt (Ser473) (#4060), Phospho-p44/42 MAPK (Erk1/2) (Thr202/Tyr204) (#9101), total Akt (#9272), p44/42 MAPK (Erk1/2) (#9102) from Cell Signaling (Leiden, The Netherlands); anti-Vinculin (V9131) from Sigma-Aldrich; HRP-conjugated anti-mouse and anti-rabbit secondary antibodies from GE Healthcare.

Preparation of genomic DNA and mRNA separation

Genomic DNA and mRNA separation was performed according to G&T-seq protocol[90]. Organoids were seeded in the platform and treated for 24 and 72 hours. At each time point, to minimize the DNA contamination of Matrigel, organoids were treated with RQ1 RNase-Free DNase (Promega, cat. no. M6101) for 30 minutes at 37°C directly by immersing the NESTs grids in the solution placed in the 348-well plate. After washes, the single matrigel drops were collected by rapid centrifugation in 50 µL of RLT plus lysis buffer (Qiagen, 1053393). Lysed cells were transferred into 200ul tubes and incubated for 20 minutes with 10 µL of oligo-dT conjugated to streptavidin beads (Invitrogen, 65001). After incubation, the poly-adenylated mRNAs

were separated using a magnet, while the DNA, present in the supernatant, was transferred to a new tube. Reverse Transcription (RT) was performed in a total volume of 5 µL of RT master mix (0,5 µL dNTP mix (Life Technologies, 18427-013), 0,05 µL Template-switching oligo (TSO; 5-AAGCAGTGGTATCAACGCAGAGTACATrGrG+G-3; IDT) 0,03 µL $MgCl_2$ (Ambion, cat. no. AM9530G), 1 µL Betaine (Sigma-Aldrich, B0300-1VL), 1 µL Superscript II first-strand buffer (Life Technologies, 18064071), 0,25 µL DTT (Life Technologies, 18064071), 0,25 µL Superscript II reverse transcriptase (Life Technologies, 18064071) and 0,12 µL RNAse inhibitor (SUPERase In, Ambion, AM2696) with the following program: 42°C for 62 min, 50°C for 30 min, 60°C for 10 min and held at 4°C. Next, the cDNA was amplified by directly adding 7.5 µL of PCR reaction mastermix (6,25 µL Kapa HiFi HotStart ReadyMix (2X) (Kapa, KK2601) and 0,12 µL IS PCR primers (5-AAGCAGTGGTATCAACGCAGAGT-3; IDT) with following thermal protocol: 98°C for 3 min; 16 cycles of 98°C for20 sec, 67°C for 15 sec and 72°C for 6 min; 72°C for 5 min and hold at 4°C. Finally, the amplified cDNA and genomic DNA (gDNA) were purified with AMPure XP beads (1X ratio) (Beckman Coulter, A63881). Quality check was performed using Tape Station platform (Agilent Technologies) in combination with Qubit High sensitivity DNA Assay Kit (Agilent Technologies, 5067-4626). DNA and RNA libraries were prepared using Nextera XT kit (Illumina, FC-131-1096) according to manufacturer's instructions. Briefly, 0.8ng of gDNA and cDNA were tagmented in 10 µL of Tagment DNA Buffer plus 5 µL of Amplicon Tagment Mix for 5 min at 55°C. The reaction was inactivated by adding 5 µL of Neutralize Tagment Buffer and incubating 5 min at room temperature. Then we added 10 µL pre-paired i7 and i5 index adapters (Illumina, IDT for Illumina DNA/RNA UD Indexes, set A and B, 20025019**,** 20025080) for each sample and 15 µL of Nextera PCR Master Mix. PCR amplification was performed with the following cycling program: 72°C for 3 min, 95°C for 30 sec, 12 cycles of 95°C for 10 sec, 55°C for 30 sec and 72°C for 30 sec; 72°C for 5 min and hold at 4°C. After library preparation, samples were purified using AMPure XP beads (1x ratio) and quality check was performed as described above. Library pools were sequenced on Novaseq 6000 (Illumina) at low coverage (0.1X; paired-end, 100 bp) for DNA and at a depth of 30 million paired-end (2X100 bp) for RNA.

Read tags were aligned to hg38 reference genome using bwa[91] (for DNA) and STAR[92] (for RNA) with default parameters. Copy Number Alterations were identified

in DNA alignments using CNVPytor[93], using variants called with bcftools[94] filtered for quality higher than 15. Genotype discordance of low pass WGS and RNA-seq with high coverage WGS was evaluated using bcftools, setting the error probability to 0, hence allowing raw comparison of the mismatched variants by their likelihood.

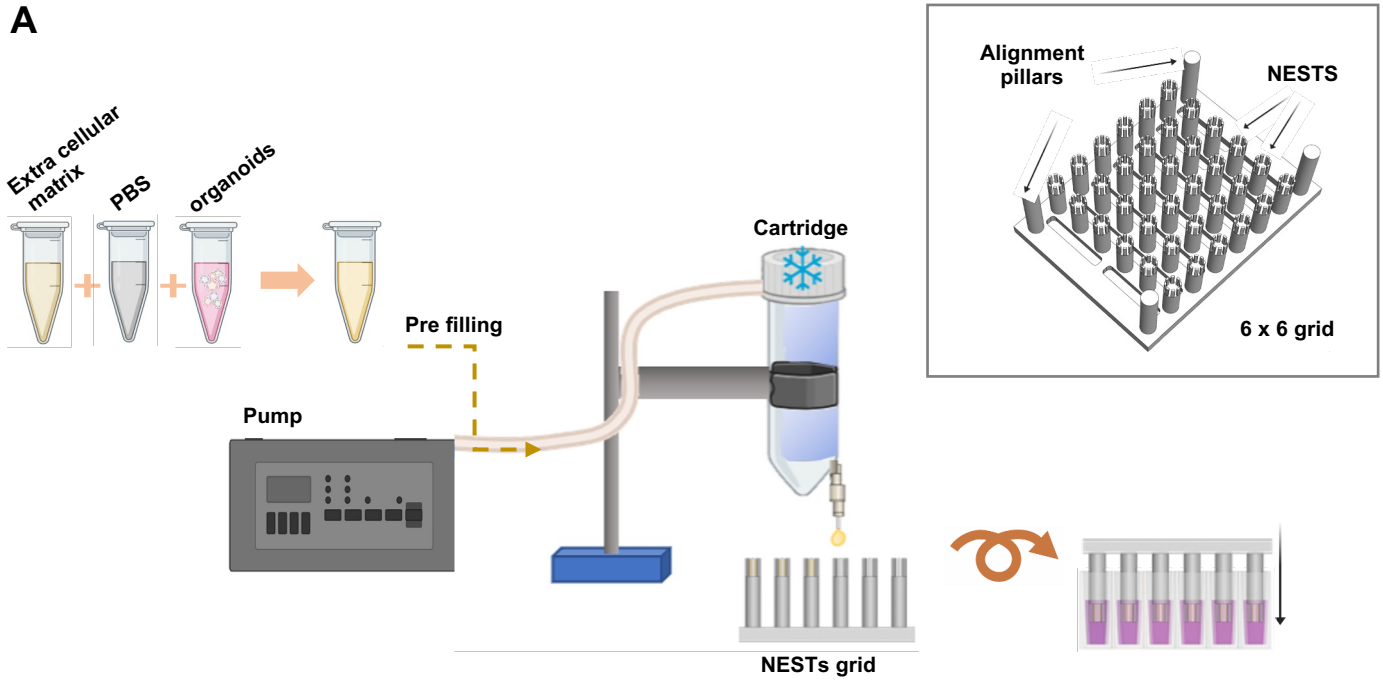
A
Extra cellular matrix
PBS
organoids
Pre filling
Pump
Cartridge
NESTs grid
Alignment pillars
NESTS
6 x 6 grid

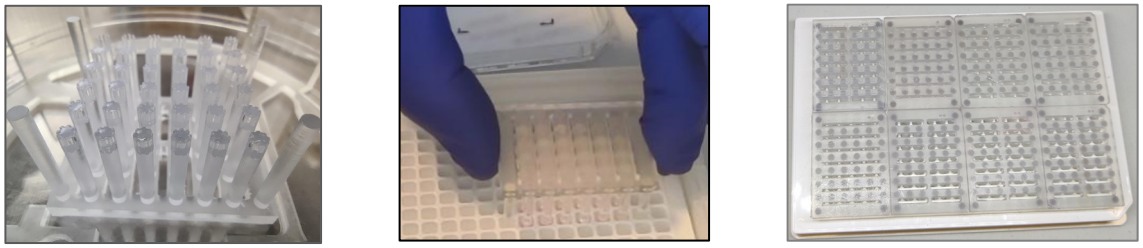
B

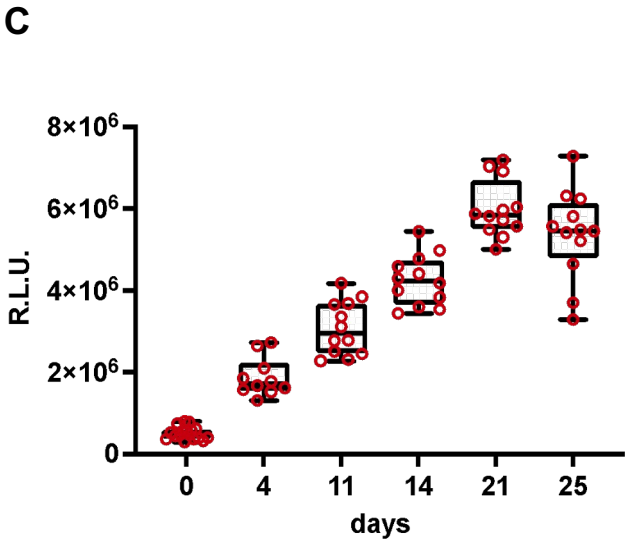
C
8×10^6
6×10^6
4×10^6
2×10^6
0
R.L.U.
0
4
11
14
21
25
days

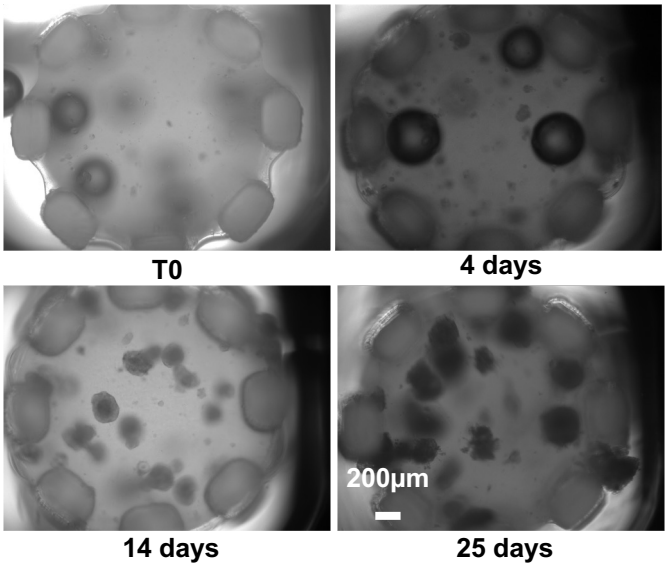
D
T0
4 days
14 days
25 days
200µm

Figure 1

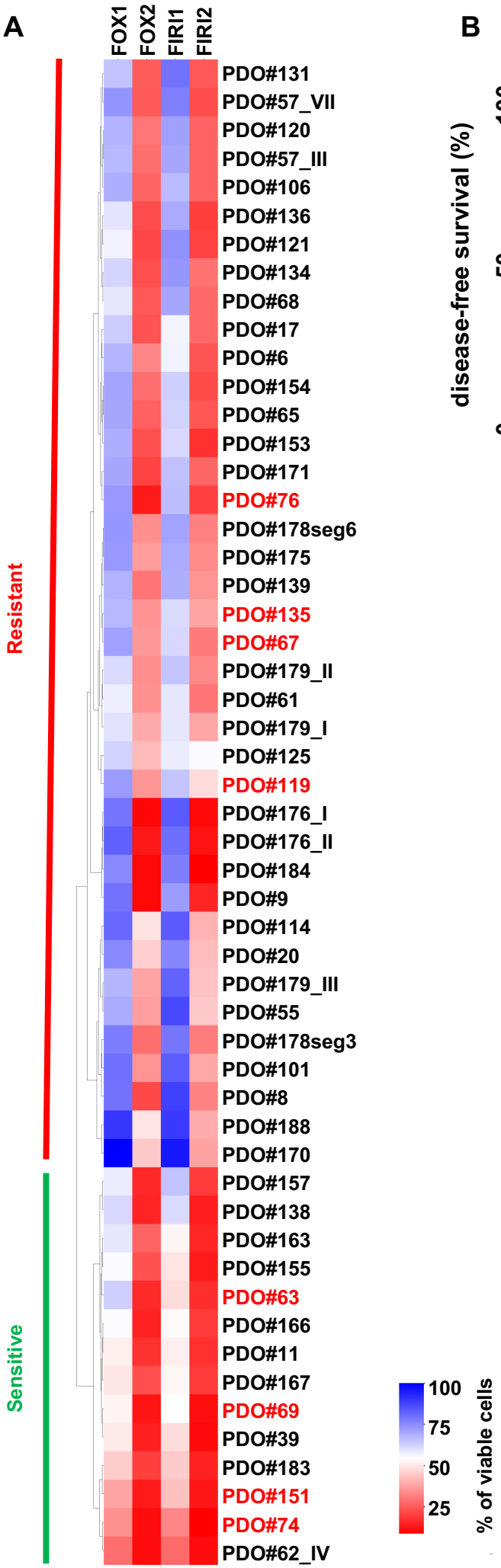
A
FOX1
FOX2
FIRI1
FIRI2
Resistant
Sensitive
PDO#131
PDO#57_VII
PDO#120
PDO#57_III
PDO#106
PDO#136
PDO#121
PDO#134
PDO#68
PDO#17
PDO#6
PDO#154
PDO#65
PDO#153
PDO#171
PDO#76
PDO#178seg6
PDO#175
PDO#139
PDO#135
PDO#67
PDO#179_II
PDO#61
PDO#179_I
PDO#125
PDO#119
PDO#176_I
PDO#176_II
PDO#184
PDO#9
PDO#114
PDO#20
PDO#179_III
PDO#55
PDO#178seg3
PDO#101
PDO#8
PDO#188
PDO#170
PDO#157
PDO#138
PDO#163
PDO#155
PDO#63
PDO#166
PDO#11
PDO#167
PDO#69
PDO#39
PDO#183
PDO#151
PDO#74
PDO#62_IV
100
75
50
25
% of viable cells

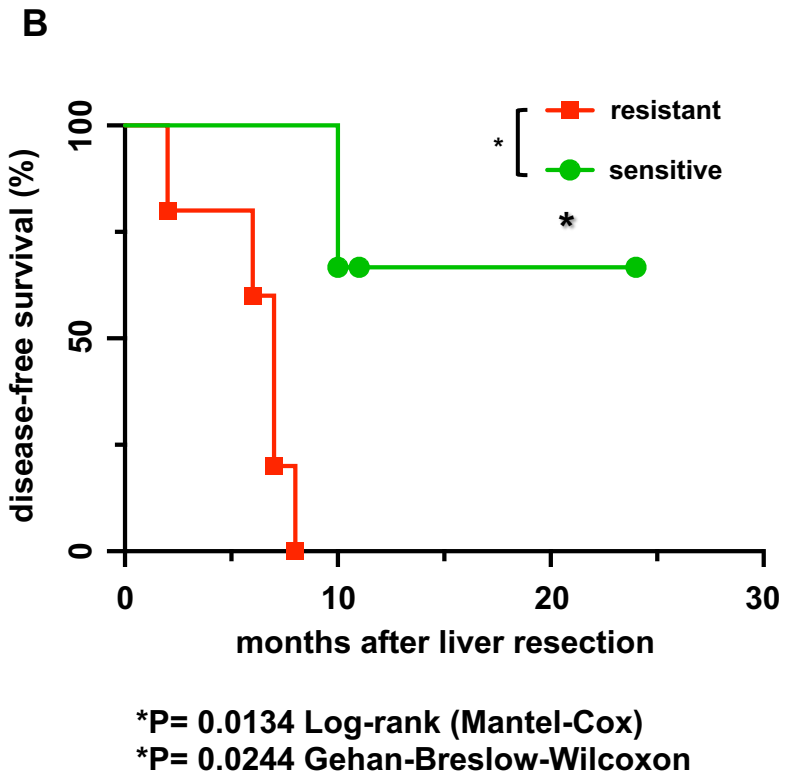
B
resistant
sensitive
*
*
disease-free survival (%)
100
50
0
0
10
20
30
months after liver resection
*P= 0.0134 Log-rank (Mantel-Cox)
*P= 0.0244 Gehan-Breslow-Wilcoxon

Figure 2

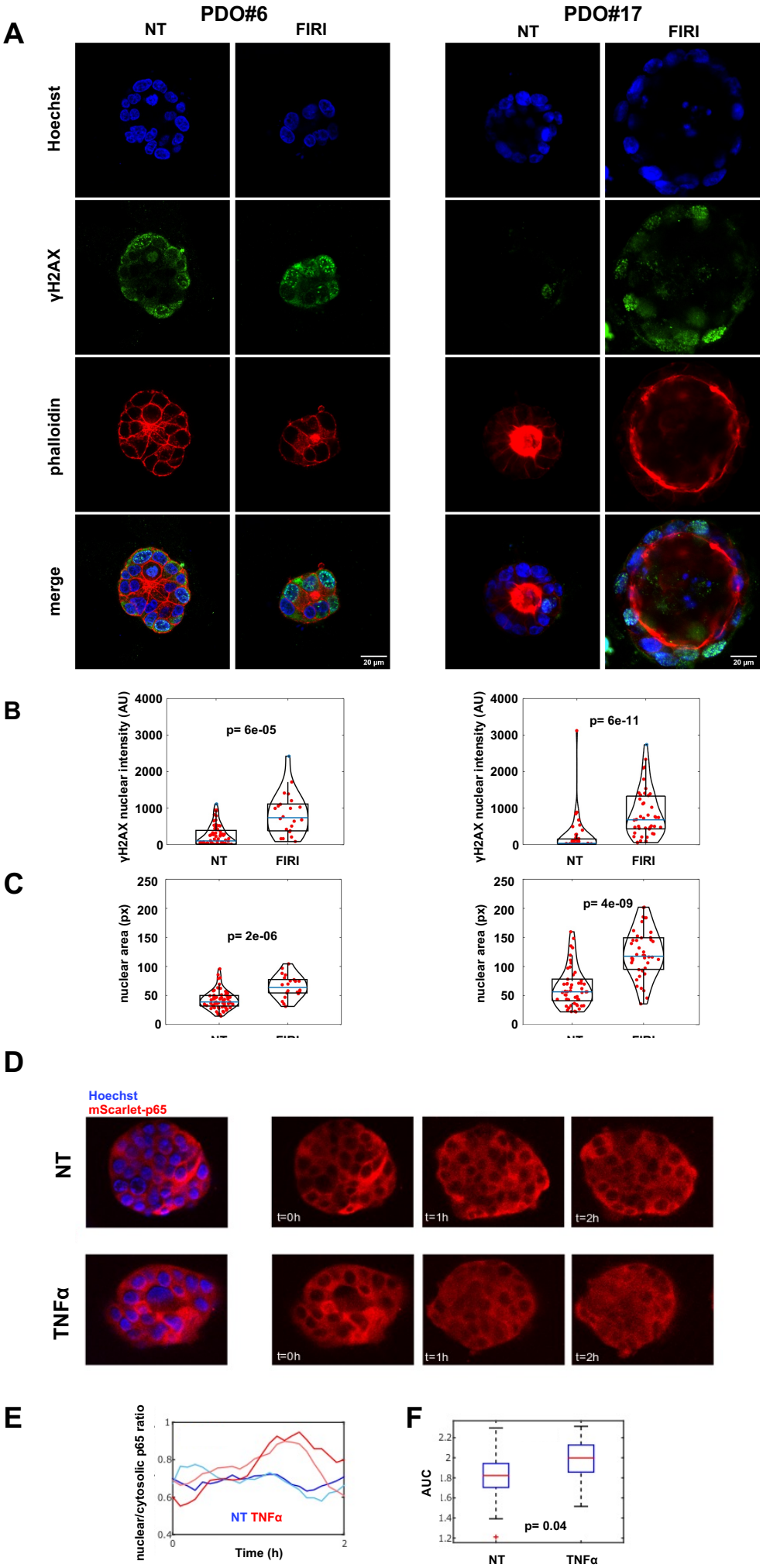
A
PDO#6
NT
FIRI
PDO#17
NT
FIRI
Hoechst
γH2AX
phalloidin
merge
20 µm
20 µm
B
γH2AX nuclear intensity (AU)
p= 6e-05
NT
FIRI
p= 6e-11
C
nuclear area (px)
p= 2e-06
p= 4e-09
D
Hoechst
mScarlet-p65
NT
TNFα
t=0h
t=1h
t=2h
E
nuclear/cytosolic p65 ratio
NT TNFα
Time (h)
F
AUC
p= 0.04
NT
TNFα

Figure 3

A

WGS on 3D platform

WGS on 24 well plate

PDO#61

PDO#62

PDO#74

RD (CN)

B

Leading logFC dim 2 (23%)

PDO#61
PDO62
PDO#74

24 h
72 h

FIRI2
FIRI1
FOX2
FOX1
NT

Leading logFC dim1 (31%)

C

Reference PDO 61

Reference PDO 62

Reference PDO 74

Average discordance

Comparison (RNA)

Figure 4

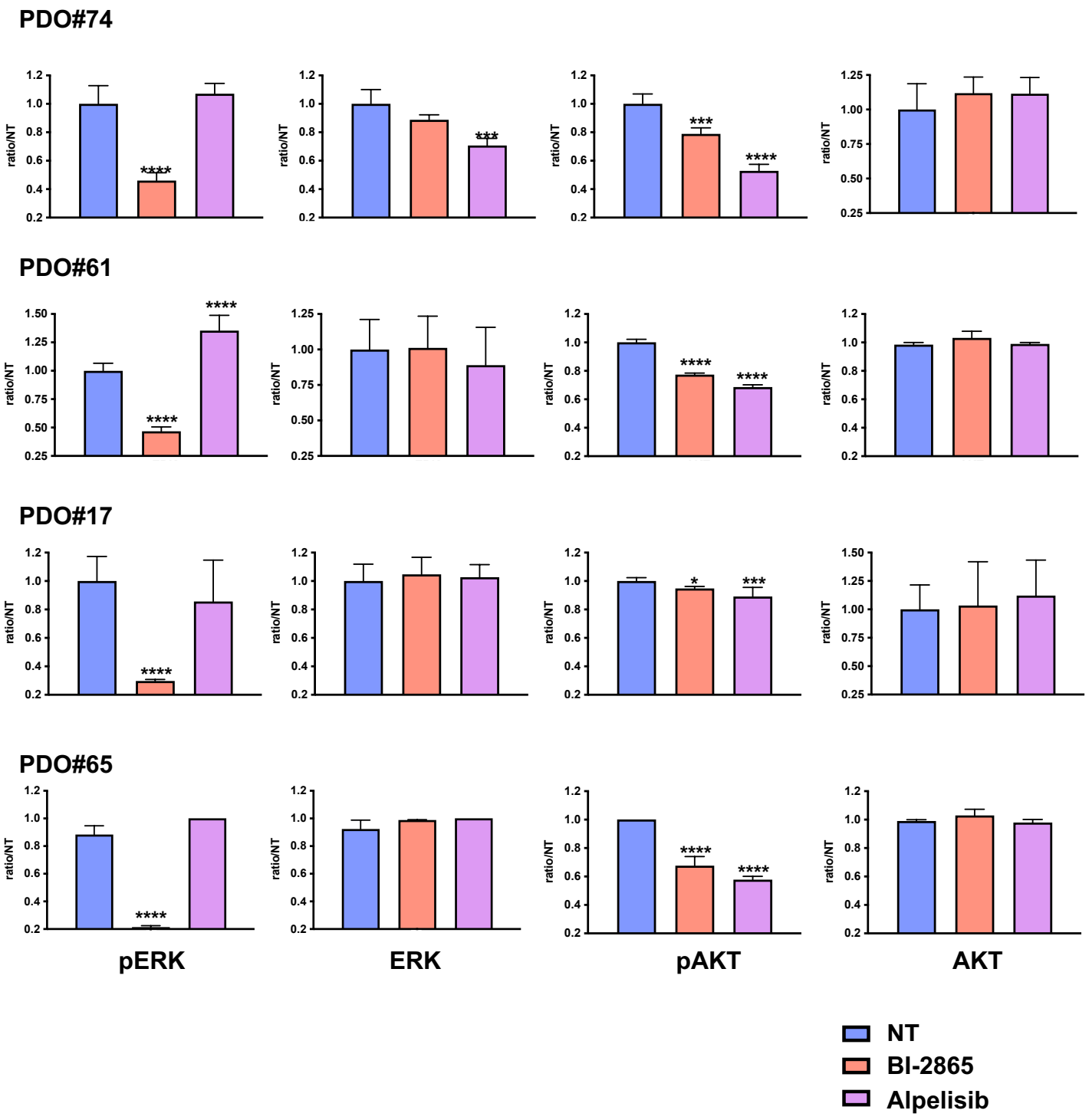
PDO#74
PDO#61
PDO#17
PDO#65
ratio/NT
pERK
ERK
pAKT
AKT
NT
BI-2865
Alpelisib

Figure 5

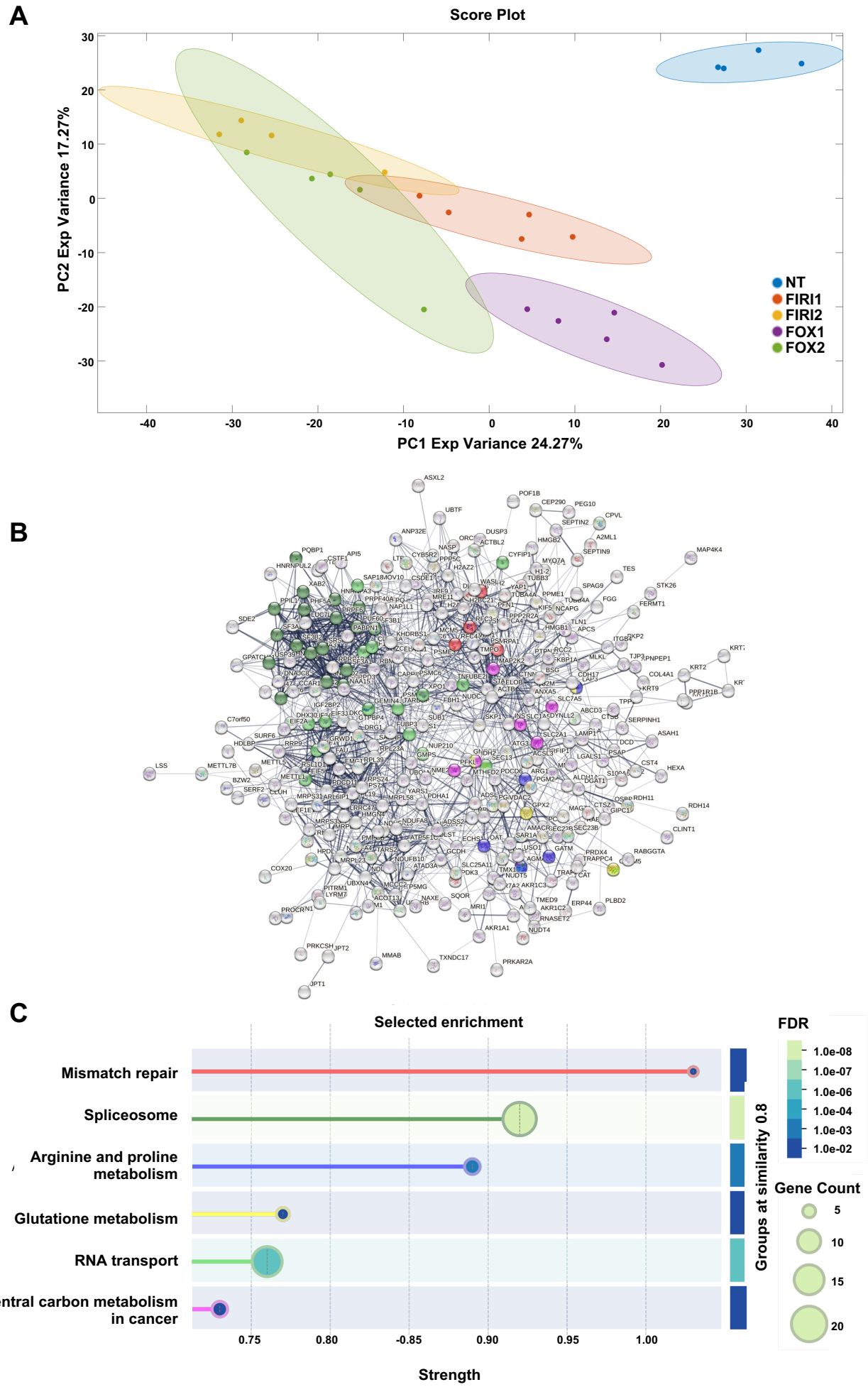
A
Score Plot
PC2 Exp Variance 17.27%
PC1 Exp Variance 24.27%
NT
FIRI1
FIRI2
FOX1
FOX2
B
C
Selected enrichment
Mismatch repair
Spliceosome
Arginine and proline metabolism
Glutatione metabolism
RNA transport
Central carbon metabolism in cancer
Strength
Groups at similarity 0.8
FDR
1.0e-08
1.0e-07
1.0e-06
1.0e-04
1.0e-03
1.0e-02
Gene Count
5
10
15
20

Figure 6

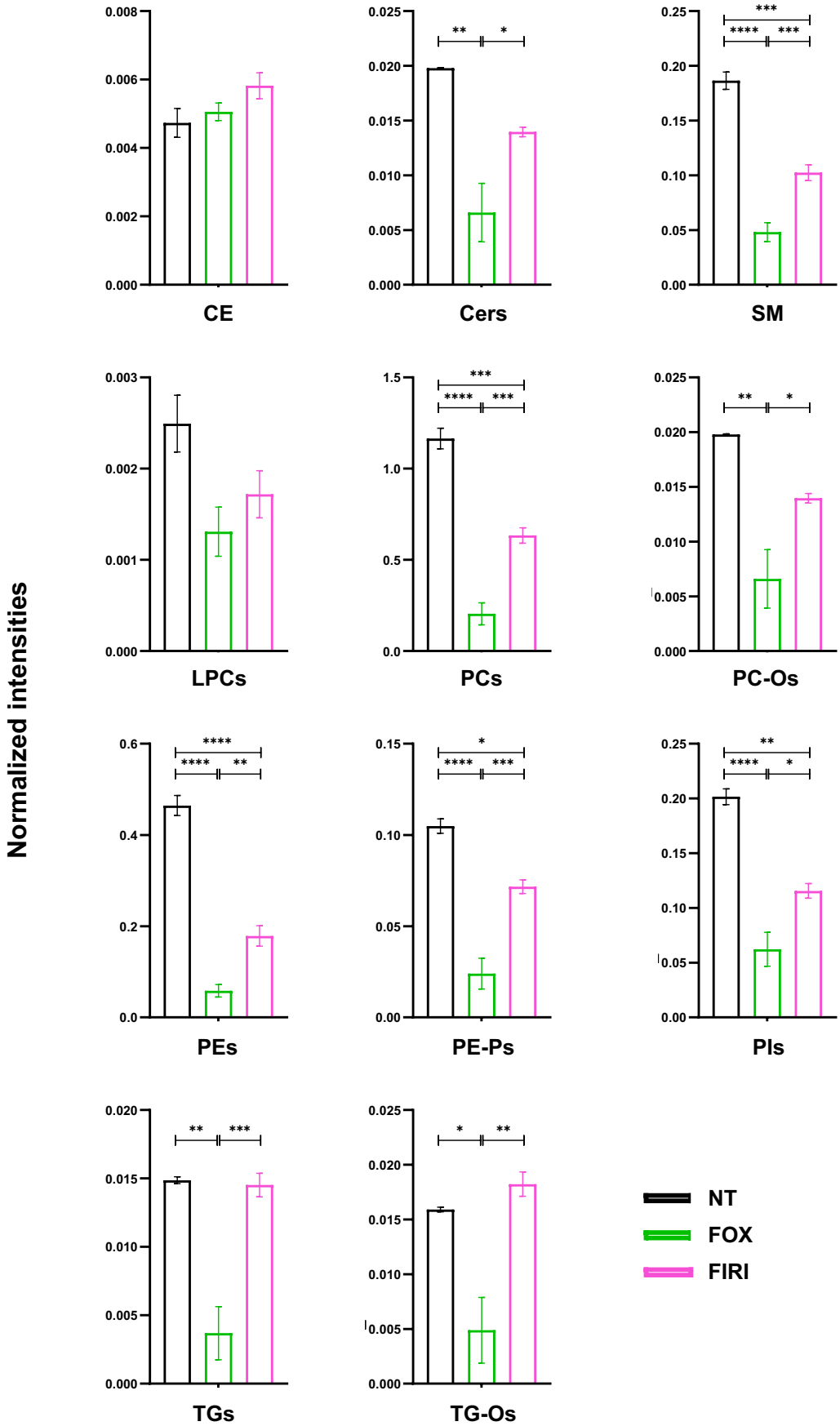
Normalized intensities
CE
Cers
SM
LPCs
PCs
PC-Os
PEs
PE-Ps
PIs
TGs
TG-Os
NT
FOX
FIRI

Figure 7